

Title: A unified explanation for the morphology of raised peatlands

Authors: Alexander R. Cobb,^{1*} René Dommain,^{2,3,4} Kimberly Yeap,⁵ Cao Hannan,⁶ Nathan C. Dadap,⁷ Bodo Bookhagen,⁸ Paul H. Glaser,⁹ Charles F. Harvey^{1,10}

Affiliations:

¹Singapore-MIT Alliance for Research and Technology; Singapore.

²Earth Observatory of Singapore, Nanyang Technological University; Singapore.

³Asian School of the Environment, Nanyang Technological University; Singapore.

⁴National Museum of Natural History, Smithsonian Institution; Washington, District of Columbia, USA.

⁵School of Civil and Environmental Engineering, Nanyang Technological University; Singapore.

⁶School of Computer Science and Engineering, Nanyang Technological University; Singapore.

⁷Department of Earth System Science, Stanford University; Stanford, California, USA.

⁸Institute of Geoscience, University of Potsdam; Potsdam, Germany.

⁹Department of Earth & Environmental Sciences, University of Minnesota; Minneapolis, Minnesota, USA.

¹⁰Department of Civil and Environmental Engineering, Massachusetts Institute of Technology; Cambridge, Massachusetts, USA.

*For correspondence: alex.cobb@smart.mit.edu

Raised peatlands, or bogs, are gently mounded landforms that are composed entirely of organic matter¹⁻⁴ and store the most carbon per area of any terrestrial ecosystem⁵. The shapes of bogs are critically important because their domed morphology^{4,6,7} accounts for much of the carbon that bogs store, and determines how they will respond to interventions^{8,9} to stop greenhouse gas emissions and fires after anthropogenic drainage¹⁰⁻¹³. However, a general theory to infer the morphology of bogs

32 is still lacking^{4,6,7}. Here we show that an equation based on the processes universal to
33 bogs explains their morphology across biomes, from Alaska, through the tropics, to New
34 Zealand. In contrast to earlier models of bog morphology that attempted only to
35 describe long-term equilibrium shapes^{4,6,7}, and were therefore inapplicable to most
36 bogs^{14–16}, our approach makes no such assumption, and makes it possible to infer full
37 shapes of bogs from a sample of elevations, such as a single elevation transect. Our
38 findings provide a foundation for quantitative inference about the morphology,
39 hydrology, and carbon storage of bogs through Earth’s history, as well as a basis for
40 planning natural climate solutions by rewetting damaged bogs around the world.

41

42 Main text

43 Bogs develop over thousands of years into distinctive mounded shapes where
44 waterlogged organic matter, or peat, decomposes more slowly than it is produced by bog
45 vegetation^{2–4,17,18}. In every bog, peat is only preserved where it is waterlogged by rain and
46 flowing water¹⁹; where peat rises too high, it cannot remain waterlogged and will decompose.
47 This mechanism constrains the height and shape of a bog^{2–4,18}. Bogs around the world differ
48 in age, environmental conditions, and organic matter composition—from the well-known
49 *Sphagnum* peat bogs of northern latitudes, to the hardwood and palm swamp peat domes of
50 the tropics, to the restiad bogs of New Zealand^{17,18,20–22}. Because of these differences, as well
51 as their irregular boundaries, each bog has a shape that is unique. Yet because of the physical
52 processes constraining their growth, the shapes of all bogs are somehow fundamentally
53 similar, opening them to systematic analysis.

54 The morphologies of bogs are important because peat is built from sequestered carbon:
55 extant peatlands have removed hundreds of gigatonnes of carbon dioxide from the

56 atmosphere over the last 10,000 years^{23,24}, cooling Earth's climate^{25,26}. However, the
57 mounded shape of bogs also makes this carbon vulnerable, because peat that is above the
58 level of streams and rivers can be drained easily by ditches and canals²⁷, exposing it to
59 decomposition and fire. Artificial drainage of peatlands now causes the emission of over
60 1.5 Pg CO₂e annually^{12,13}, and enables catastrophic fires and smoke that have caused
61 hundreds of thousands of premature deaths^{10,11}. Rewetting of peatlands could stop these
62 greenhouse gas emissions and fires^{13,19,28}, and has been identified as one of the most
63 promising nature-based strategies for meeting global climate targets set by the 2015 United
64 Nations Framework Convention on Climate Change (UNFCCC) Paris Agreement^{13,29,30}.
65 However, mitigation by rewetting cannot be planned effectively without understanding
66 peatland morphology and water flow patterns.

67 The morphology and flow patterns of bogs are difficult to measure directly because
68 elevation gradients are small compared to local microtopography and vegetation^{7,20,31}.
69 Peatland elevation gradients can be resolved by methods such as airborne lidar³¹, but these
70 methods are expensive³² and the global area of peatlands is vast^{23,33}. Thus, an understanding
71 of the morphology of bogs is important both for evaluating their role in the Earth system
72 through time, and also for planning climate mitigation measures in raised peatlands. Although
73 models exist for some restricted conditions, no general, quantitative theory has been available
74 to infer raised bog morphology and flow patterns from limited data.

75 Here we show that because all raised peatlands are governed by the same essential
76 processes, there is a common pattern in bog morphologies that holds irrespective of many
77 site- and ecosystem-dependent factors (Figs. 1 and 2). Because of this pattern, the
78 complexities created by the irregular geometry of bog boundaries can be accounted for in a
79 unified way across all bogs, while the site- and ecosystem-specific aspects are described by a
80 single site-specific function. The separate treatment of geometric and site-specific factors is

81 an approximation; however, we show by analysis and eight examples of bogs from boreal,
82 temperate, and tropical regions that it is accurate in a wide range of cases. This approach
83 makes it feasible to characterise, from limited data, the overall morphology and hydrology of
84 bogs thousands of hectares in size. As an example, we show that the full shape of bogs can be
85 estimated with high accuracy from a single elevation transect. Our analysis greatly amplifies
86 the range of inference that can be made from measurements in raised bogs and opens the way
87 for interpretation of sparse data on bogs from Earth's deep history^{34–36}, as well as many
88 extant bogs in remote parts of the Amazon Basin, New Guinea, and the Congo Basin that are
89 already threatened by development but remain poorly known scientifically^{33,37,38}.

90 We derive our equation for the morphology of bogs by observing that the similarity in
91 their shapes across biomes arises from the constraint that peat must be waterlogged to be
92 preserved, and therefore bog morphology is governed indirectly by the physics controlling
93 the water table^{4,6,7,39}. Bog water tables are controlled by the balance between net precipitation
94 and discharge by lateral flow; lateral flow is controlled by the gradient in the water table
95 times the efficiency of this flow, or transmissivity, which arises from the hydraulic properties
96 of the peat³⁹. The hydraulic properties of peat vary strongly with depth but tend to be uniform
97 at a large scale across a bog^{4,40–42}. These observations suggest that bog surface elevation,
98 mean water table elevation, and transmissivity are related to one another in similar ways
99 across a bog. In that case, analysis (Methods) shows that the relationships among these
100 variables define a bog-specific monotonic function $p(\phi)$ that generates the bog morphology
101 $p(x,y)$ from a solution to Poisson's equation $-\nabla^2\phi = k$ where k is a constant (defined for
102 convenience as $8\pi \text{ km}^{-2}$; Methods). While the dimensionless Poisson "elevation" $\phi(x,y)$
103 represents an abstract reference morphology for the bog, the bog-function $p(\phi)$ summarises
104 the climate- and ecosystem-specific relationship between surface elevation, mean water table
105 elevation, and transmissivity that transforms the abstract reference morphology $\phi(x,y)$ into

106 actual bog surface elevations p . This formulation splits the complex morphology of raised
107 peatlands into (1) what is universal to all bogs: the existence of a monotonic relationship
108 between bog surface elevation and the solution to Poisson's equation inside each bog's
109 boundary; and (2) what is specific to a bog: the shape of the bog's boundary in three-
110 dimensional space and a one-dimensional bog-function.

111 Elevation data from sites around the world are consistent with this theory. Applying
112 this analysis to eight bogs from boreal, temperate, and tropical latitudes (Fig. 2)—at Hamilton
113 Bay (Alaska, USA), Milot (Quebec, Canada), Great Cranberry Island (Maine, USA),
114 Valgeraba (Estonia), Mendaram (Brunei Darussalam), Kopuatai (New Zealand), Reksuo
115 (Finland), and Lost River (Minnesota, USA)—we find strong rank-correlation between
116 Poisson elevations ϕ and lidar-derived elevations covering the whole surface of each bog ($\rho \geq$
117 0.92; Fig. 1). Rank-correlation means that, despite scatter caused by measurement error and
118 small-scale deviations in elevation, surface elevation increases monotonically with Poisson
119 elevation, as hypothesised. Transforming the Poisson solution through a monotonic function
120 $p(\phi)$ (Methods) then closely reproduces the lidar morphology, with high coefficients of
121 determination (elevation $R^2 \geq 0.84$), root-mean-square differences comparable to the noise in
122 the lidar terrain data (RMSE ≤ 27.6 cm), and small biases (≤ 0.1 mm). This agreement
123 between theory- and lidar-derived surface elevations shows that the one-dimensional bog-
124 function, in combination with the shape of the bog boundary, effectively describes the full
125 three-dimensional shape of each bog (Fig. 1 and Extended Data Fig. 1).

126 Our equation subsumes and extends existing models describing bog morphology^{4,6,7}.
127 Each of these models effectively assumes a particular fixed relationship between water level,
128 transmissivity, and peat surface elevation, resulting in a particular form of the bog-function,
129 and therefore our approach includes them as special cases. In the model presented by Ivanov
130 and later Ingram,^{4,6} the transmissivity at any point in a bog is proportional to the peat surface

131 elevation above a flat surface, whereas the model of Cobb et al. (2017)⁷ assumes that flow
132 occurs predominantly near the surface and that time-averaged transmissivity is uniform. The
133 applicability of these models is limited to computing equilibrium morphologies in which a
134 bog is neither gaining nor losing peat with time, whereas radiocarbon and carbon flux
135 measurements show that most bogs are either actively losing or sequestering carbon,^{14–16}
136 which results in more complex bog-functions (Extended Data Fig. 2). Nonetheless, our
137 approach accommodates either of these equilibrium models or anything in between, as we
138 illustrate by calculating the morphology of an arbitrarily shaped bog with a transmissivity
139 that starts at a constant and increases towards the bog interior, where mean water table
140 elevations are higher (Fig. 3). As this example demonstrates, besides describing the shape of
141 real bogs, our approach can also generate morphologies conforming to existing or more
142 general models. We next show that by combining these capabilities, we can infer the
143 morphology of bogs from limited data.

144 To show how our equation can support inference about bog morphology, we evaluated
145 our method's ability to recover the full shape of a bog from a single elevation transect. Our
146 analysis implies that the function $p(\phi)$ that transforms Poisson elevations to bog surface
147 elevations is the same throughout the bog, and thus that the full bog morphology can be
148 estimated from a sample of elevations, such as a single elevation transect. We sampled
149 elevations along the same transects shown in Fig. 1—used there to illustrate goodness-of-
150 fit—to determine bog-functions and full bog morphologies. For each bog, we solved
151 Poisson's equation within the bog boundary, sampled elevations along the transect, and used
152 the function relating the two to transform Poisson elevations to an overall bog morphology.
153 This approach predicted surface elevations and flow patterns in parts of the bog that were not
154 sampled at all, and resulted in remarkable fidelity to overall bog morphology. Thus, one

155 important application of our analysis is to estimate the overall morphology of a raised bog
156 from the shape of its boundary and a single transect of surface elevations (Fig. 4).

157 By enabling the estimation of bog morphologies from limited data, the bog-function
158 approach also enables estimation of the spatially concentrated and climate-action-critical^{5,43}
159 irrecoverable carbon stored in bogs. Irrecoverable carbon is defined as carbon that is
160 vulnerable to loss in a typical land-use change event and that cannot be recovered by
161 restoration efforts on timescales relevant for climate action (by mid-century).^{30,43} Raised bogs
162 are typically drained for agriculture by a grid of ditches or subsurface drains^{8,20,27,44–46} that are
163 progressively deepened as peat is lost to decomposition or fire^{20,47} until the bog is no longer
164 drainable by this approach and the bog surface is no longer raised. Subtracting this limiting
165 horizon of passive drainability from the bog surface morphology (Methods) yields the
166 volume of peat that is vulnerable to this type of land-use change event. This peat volume,
167 multiplied by an appropriate carbon density (Methods), yields the vulnerable peat carbon in
168 the bog. In this way the bog-function approach makes it possible to estimate the irrecoverable
169 carbon held by a bog using elevations from the bog boundary and a single elevation transect
170 (Fig. 4).

171 Our equation is based on the approximation that bog surface elevation, water level, and
172 transmissivity have a consistent relationship across a bog (Methods). The most important
173 reason these links might vary within a bog is because of recent changes to the drainage
174 network or the peat surface by land use, for example by peat mining⁸. Thus, more work will
175 be required to explore the application of our analysis in recently altered bogs. For example, in
176 bogs cut by ditches, the bog may need to be split into two or more domains and our method
177 applied independently in each (e.g., Lost River, Extended Data Fig. 1). However, the peat
178 surface and the water table will tend to converge back towards one another with time.
179 Therefore, if the alteration was made some time ago our analysis can still be highly accurate:

180 the bogs we analysed at Lost River, Reksuo, Valgeraba, Mendaram and Kopuatai are all
181 affected by drainage at their margins (Figs. 1, 4, Extended Data Figs. 1 and 3) but still fit our
182 theory, with coefficients of determination of at least 84% (Figs. 1, 4 and Extended Data Fig.
183 1).

184 This scheme for inference about bog morphology and hydrology has applications and
185 benefits across a range of fields. As just demonstrated, it provides a morphological theory for
186 extant peatlands that can be used to infer the shape of bogs from limited data, and thus to
187 quantify the carbon at risk of being released if a bog is drained, or carbon dioxide emissions
188 that will be avoided if it is protected. From elevation transects we were able to estimate the
189 irrecoverable carbon stored in bogs ranging in mass from 1.45 Gg C (Hamilton Bay, 0.06
190 km²) to 3.07 Pg C (Mendaram, 24.5 km²) with errors of less than 6% (Fig. 4k). When total
191 peat volume, including peat safely sequestered below the drainability horizon, is desired, bog
192 surface topography can be combined with a sample of peat depths to yield total peat volume
193 due to a widely observed empirical correlation between peat surface elevation and peat
194 thickness⁴⁸ (Methods). Inferred bog shapes also provide maps of gradients in the peat surface
195 elevation, as required for optimal dam placement when rewetting peatlands for climate
196 mitigation^{9,49}. Maps of bog elevations and gradients are needed as well for prediction of peat
197 saturation and flooding after rewetting, both to forecast methane emissions, which can
198 counteract carbon dioxide emission reductions¹⁹, and to plan revegetation with sensitive
199 wetland species^{8,50}. Our approach can also be used to determine contributing areas and model
200 flow in undergauged catchments, relevant in settings where peatlands contribute significantly
201 to drinking water supplies⁵¹ or flood risk⁵². Finally, by relating bog morphology to
202 hydrological processes, our theory enables previously impossible palaeohydrological and
203 palaeoecological interpretation of buried and fossil peatlands^{34–36,53}, such as the vast coal
204 fields of the Eastern Interior Basin in North America⁵⁴.

205 Our analysis provides a unifying framework for inference about raised peatland
206 morphology and hydrological processes that applies to raised bogs globally, from boreal, to
207 tropical, and further to southern temperate regions. The equation we derive handles the
208 complexity arising from the irregular boundaries of bogs in a uniform way, while accounting
209 for the diversity of processes in bogs by a site-specific function, capturing both how all bogs
210 are similar, and how they are different. It thus provides a foundation for understanding
211 landforms that have been a major part of the Earth system since the Carboniferous³⁴, and now
212 have immediate practical importance because of large greenhouse gas and smoke emissions
213 from drained peatlands^{10–13,19} that, if reversed, could make global climate goals
214 achievable^{13,29,30}.

215 **Main references**

- 216 1. Molengraaff, G. A. F. *Borneo Expeditie—Geologische Verkenningstochten in Centraal-*
217 *Borneo (1893–94) (Borneo expedition—Geological reconnaissance in central Borneo*
218 *(1893–94)* (H. Gerlings, Amsterdam, The Netherlands, 1900).
- 219 2. Weber, C. A. *Über die Vegetation und Entstehung des Hochmoors von Augstimal im*
220 *Memeldelta mit vergleichenden Ausblicken auf andere Hochmoore der Erde; Eine*
221 *formationsbiologisch-historische und geologische Studie* (Paul Parey, Berlin, Prussia,
222 1902).
- 223 3. Granlund, E. De svenska högmossarnas geologi. *Sveriges Geologiska Undersökningar*
224 **26**, 1–93 (1932).
- 225 4. Ivanov, K. E. *Water movement in mirelands* (Academic Press, London, UK, 1981).
226 Translated from the Russian text *Voddoobmen v blotnykh lanshaftakh* by A. Thomson and
227 H. A. P. Ingram.

- 228 5. Temmink, R. J. M. et al. Recovering wetland biogeomorphic feedbacks to restore the
229 world's biotic carbon hotspots. *Science* **376**, (2022).
- 230 6. Ingram, H. A. P. Size and shape in raised mire ecosystems: A geophysical model. *Nature*
231 **297**, 300–303 (1982).
- 232 7. Cobb, A. R. et al. How temporal patterns in rainfall determine the geomorphology and
233 carbon fluxes of tropical peatlands. *Proceedings of the National Academy of Sciences of*
234 *the United States of America* **114**, E5187–E5196 (2017).
- 235 8. Price, J. S., Heathwaite, A. L. & Baird, A. J. Hydrological processes in abandoned and
236 restored peatlands: An overview of management approaches. *Wetlands Ecology and*
237 *Management* **11**, 65–83 (2003).
- 238 9. Ritzema, H., Limin, S., Kusin, K., Jauhiainen, J. & Wösten, H. Canal blocking strategies
239 for hydrological restoration of degraded tropical peatlands in Central Kalimantan,
240 Indonesia. *Catena* **114**, 11–20 (2014).
- 241 10. Johnston, F. H. et al. Estimated global mortality attributable to smoke from landscape
242 fires. *Environmental Health Perspectives* **120**, 695–701 (2012).
- 243 11. Koplitz, S. N. et al. Public health impacts of the severe haze in Equatorial Asia in
244 September–October 2015: Demonstration of a new framework for informing fire
245 management strategies to reduce downwind smoke exposure. *Environmental Research*
246 *Letters* **11**, 094023 (2016).
- 247 12. Miettinen, J., Hooijer, A., Vernimmen, R., Liew, S. C. & Page, S. E. From carbon sink to
248 carbon source: Extensive peat oxidation in insular Southeast Asia since 1990.
249 *Environmental Research Letters* **12**, 024014 (2017).
- 250 13. Leifeld, J., Wüst-Galley, C. & Page, S. Intact and managed peatland soils as a source and
251 sink of GHGs from 1850 to 2100. *Nature Climate Change* **9**, 945–947 (2019).

- 252 14. Limpens, J. et al. Peatlands and the carbon cycle: From local processes to global
253 implications – a synthesis. *Biogeosciences* **5**, 1475–1491 (2008).
- 254 15. Lund, M. et al. Variability in exchange of CO₂ across 12 northern peatland and tundra
255 sites. *Global Change Biology* **16**, 2436–2448 (2010).
- 256 16. Hirano, T., Jauhiainen, J., Inoue, T. & Takahashi, H. Controls on the carbon balance of
257 tropical peatlands. *Ecosystems* **12**, 873–887 (2009).
- 258 17. Gorham, E. The development of peat lands. *The Quarterly Review of Biology* **32**, 145–
259 166 (1957).
- 260 18. Anderson, J. A. R. The structure and development of the peat swamps of Sarawak and
261 Brunei. *Journal of Tropical Geography* **18**, 7–16 (1964).
- 262 19. Evans, C. D. et al. Overriding water table control on managed peatland greenhouse gas
263 emissions. *Nature* **593**, 548–552 (2021).
- 264 20. Rydin, H. & Jeglum, J. *The biology of peatlands*. (Oxford University Press, 2006).
- 265 21. Läähteenoja, O., Flores, B. & Nelson, B. Tropical peat accumulation in Central Amazonia.
266 *Wetlands* **33**, 495–503 (2013).
- 267 22. Dargie, G. C. et al. Congo Basin peatlands: Threats and conservation priorities.
268 *Mitigation and Adaptation Strategies for Global Change* **24**, 669–686 (2019).
- 269 23. Gorham, E. Northern peatlands: Role in the carbon cycle and probable responses to
270 climatic warming. *Ecological Applications* **1**, 182–195 (1991).
- 271 24. Yu, Z., Loisel, J., Brosseau, D. P., Beilman, D. W. & Hunt, S. J. Global peatland
272 dynamics since the Last Glacial Maximum. *Geophysical Research Letters* **37**, (2010).
- 273 25. Frohling, S. et al. Peatlands in the Earth’s 21st century climate system. *Environmental*
274 *Reviews* **19**, 371–396 (2011).

- 275 26. Dommain, R. et al. A radiative forcing analysis of tropical peatlands before and after their
276 conversion to agricultural plantations. *Global Change Biology* **24**, 5518–5533 (2018).
- 277 27. Ritzema, H. P., ed. *Drainage principles and applications*. (International Institute for Land
278 Reclamation; Improvement, 1994).
- 279 28. Turetsky, M. R. et al. Global vulnerability of peatlands to fire and carbon loss. *Nature*
280 *Geoscience* **8**, 11–14 (2014).
- 281 29. Morecroft, M. D. et al. Measuring the success of climate change adaptation and
282 mitigation in terrestrial ecosystems. *Science* **366**, eaaw9256 (2019).
- 283 30. Goldstein, A. et al. Protecting irrecoverable carbon in Earth’s ecosystems. *Nature Climate*
284 *Change* **10**, 287–295 (2020).
- 285 31. Korpela, I., Koskinen, M., Vasander, H., Holopainen, M. & Minkkinen, K. Airborne
286 small-footprint discrete-return LiDAR data in the assessment of boreal mire surface
287 patterns, vegetation, and habitats. *Forest Ecology and Management* **258**, 1549–1566
288 (2009).
- 289 32. Vernimmen, R. et al. Creating a lowland and peatland landscape digital terrain model
290 (DTM) from interpolated partial coverage LiDAR data for Central Kalimantan and East
291 Sumatra, Indonesia. *Remote Sensing* **11**, 1152 (2019).
- 292 33. Warren, M., Hergoualc’h, K., Kauffman, J. B., Murdiyarso, D. & Kolka, R. An appraisal
293 of Indonesia’s immense peat carbon stock using national peatland maps: Uncertainties
294 and potential losses from conversion. *Carbon Balance and Management* **12**, (2017).
- 295 34. Greb, S. F., DiMichele, W. A. & Gastaldo, R. A. Evolution and importance of wetlands in
296 earth history. in *Wetlands through time* (eds. Greb, S. F. & DiMichele, W. A.) 1–40
297 (Geological Society of America, 2006).

- 298 35. Morley, R. J. Cenozoic ecological history of South East Asian peat mires based on the
299 comparison of coals with present day and Late Quaternary peats. *Journal of Limnology*
300 **72**, 36–59 (2013).
- 301 36. Treat, C. C. et al. Widespread global peatland establishment and persistence over the last
302 130,000 y. *Proceedings of the National Academy of Sciences* **116**, 4822–4827 (2019).
- 303 37. Crezee, B. et al. Mapping peat thickness and carbon stocks of the central Congo Basin
304 using field data. *Nature Geoscience* **15**, 639–644 (2022).
- 305 38. Hastie, A. et al. Risks to carbon storage from land-use change revealed by peat thickness
306 maps of Peru. *Nature Geoscience* **15**, 369–374 (2022).
- 307 39. Childs, E. C. & Youngs, E. G. A study of some three-dimensional field-drainage
308 problems. *Soil Science* **92**, 15–24 (1961).
- 309 40. Baird, A. J. et al. High permeability explains the vulnerability of the carbon store in
310 drained tropical peatlands. *Geophysical Research Letters* **44**, 1333–1339 (2017).
- 311 41. Cobb, A. R. & Harvey, C. F. Scalar simulation and parameterization of water table
312 dynamics in tropical peatlands. *Water Resources Research* **55**, 9351–9377 (2019).
- 313 42. Morris, P. J., Baird, A. J., Eades, P. A. & Surridge, B. W. J. Controls on near-surface
314 hydraulic conductivity in a raised bog. *Water Resources Research* **55**, 1531–1543 (2019).
- 315 43. Noon, M. L. et al. Mapping the irrecoverable carbon in Earth’s ecosystems. *Nature*
316 *Sustainability* **5**, 37–46 (2021).
- 317 44. Tay, T. H. The distribution, characteristics, uses and potential of peat in West Malaysia.
318 *Journal of Tropical Geography* **29**, 58–63 (1969).

- 319 45. Lim, K. H., Lim, S. S., Parish, F. & Suharto, R., eds. *RSPO manual on Best Management*
320 *Practices (BMPs) for existing oil palm cultivation on peat*. (Roundtable on Sustainable
321 Palm Oil, 2012).
- 322 46. Holden, J., Chapman, P. J. & Labadz, J. C. Artificial drainage of peatlands: Hydrological
323 and hydrochemical process and wetland restoration. *Progress in Physical Geography* **28**,
324 95–123 (2004).
- 325 47. Andriessse, J. P. Nature and management of tropical peat soils. *FAO Soils Bulletin* **59**,
326 (1988).
- 327 48. Silvestri, S. et al. Quantification of peat thickness and stored carbon at the landscape scale
328 in tropical peatlands: A comparison of airborne geophysics and an empirical topographic
329 method. *Journal of Geophysical Research: Earth Surface* **124**, 3107–3123 (2019).
- 330 49. Parry, L. E., Holden, J. & Chapman, P. J. Restoration of blanket peatlands. *Journal of*
331 *Environmental Management* **133**, 193–205 (2014).
- 332 50. Dommain, R. et al. Ecosystem services, degradation and restoration of peat swamps in the
333 South East Asian tropics. in *Peatland restoration and ecosystem services* (eds. Bonn, A.,
334 Allott, T., Evans, M., Joosten, H. & Stoneman, R.) 253–288 (Cambridge University
335 Press, 2016).
- 336 51. Martin-Ortega, J., Allott, T. E. H., Glenk, K. & Schaafsma, M. Valuing water quality
337 improvements from peatland restoration: Evidence and challenges. *Ecosystem Services* **9**,
338 34–43 (2014).
- 339 52. Hidayat, H., Hoekman, D. H., Vissers, M. A. M. & Hoitink, A. J. F. Flood occurrence
340 mapping of the middle Mahakam lowland area using satellite radar. *Hydrology and Earth*
341 *System Sciences* **16**, 1805–1816 (2012).

- 342 53. Cecil, C. B. et al. Paleoclimate controls on Late Paleozoic sedimentation and peat
343 formation in the central Appalachian basin (U.S.A.). *International Journal of Coal*
344 *Geology* **5**, 195–230 (1985).
- 345 54. Greb, S. F. et al. Desmoinesian coal beds of the Eastern Interior and surrounding basins:
346 The largest tropical peat mires in Earth history. in *Extreme depositional environments:*
347 *Mega end members in geologic time* (eds. Chan, M. A. & Archer, A. W.) 127–150
348 (Geological Society of America, Boulder, Colorado, USA, 2003).
- 349 55. Fick, S. E. & Hijmans, R. J. WorldClim 2: New 1-km spatial resolution climate surfaces
350 for global land areas. *International Journal of Climatology* **37**, 4302–4315 (2017).
- 351 56. Xu, J., Morris, P. J., Liu, J. & Holden, J. PEATMAP: Refining estimates of global
352 peatland distribution based on a meta-analysis. *Catena* **160**, 134–140 (2018).
- 353 57. Korhola, A. A. Radiocarbon evidence for rates of lateral expansion in raised mires in
354 southern Finland. *Quaternary Research* **42**, 299–307 (1994).

355 **Main figure legends**

356 **Fig. 1. Monotonic relationship between bog morphology and solution to Poisson's**

357 **equation in global peatlands. (a)** Bog name, location, and major peat-forming vegetation.

358 See Fig. 2 for map of bog locations. **(b)** Irrecoverable carbon³⁰ in the bog: carbon that would

359 be vulnerable to loss in a typical land-use change event and cannot be recovered on climate-

360 relevant timescales (Methods). **(c)** Boundary used when approximating bog morphology in

361 **(f).** Satellite images: CNES / Airbus, Google, Landsat / Copernicus, Maxar Technologies,

362 TerraMetrics. **(d)** Map of peat surface elevations measured by lidar, in metres above sea level

363 (light grey lines: contours; white arrows: flowlines). **(e)** All surface elevations from **(d)**

364 plotted against the value of the solution to Poisson's equation at the same location within the

365 bog (blue points), showing Spearman's rank correlation coefficient ρ . The bog-function

366 (black line) was obtained by rank regression (Methods). **(f)** Approximate surface elevations

367 from transforming the solution to Poisson's equation using the bog-function shown in **(e)**.

368 The correspondence with measured elevations **(d)** is shown by the coefficient of

369 determination R^2 . **(g)** Surface elevations from lidar **(d)**; blue points) and from our theory **(f)**;

370 black curves) along the transect shown as a dashed line in **(f)**.

371 **Fig. 2. Distribution of bog sites in geographic and climate space. (a)** Site locations, mean

372 annual temperature⁵⁵, and global peatland distribution (brown, ref.⁵⁶). **(b)** Sites, literature

373 peatland sites (brown, ref.³⁶), and global land surface (grey) in "climate space" of mean

374 annual temperature and precipitation; permafrost areas (light blue) are not considered in this

375 study.

376 **Fig. 3. The bog-function approach subsumes existing models of bog morphology.**

377 Besides describing natural bogs (Fig. 1), our approach can also generate equilibrium

378 morphologies for bogs according to the existing models of Ivanov / Ingram^{4,6} or Cobb et al.

379 (2017),⁷ because these correspond to particular forms for the bog-function. **(a)** Hybrid
380 example intermediate between the models of Ivanov and Ingram^{4,6} and of Cobb et al. (2017).⁷
381 Gaussian noise has been added to the peat surface elevation to mimic microtopographic
382 features typical in peatlands. **(b)** Cross-section of generated morphology. **(c)** In this example,
383 time-averaged hydraulic transmissivity is set to a constant at the bog margin and then
384 increases linearly with average water table elevation: this is a mixture of the equilibrium
385 models of Ivanov and Ingram,^{4,6} wherein transmissivity increases linearly from zero at the
386 bog margin, and Cobb et al. (2017)⁷ wherein time-averaged transmissivity is approximately
387 uniform. **(d)** We include a trend in water level relative to the peat surface towards the bog
388 interior, which is not accommodated by these earlier models. **(e)** Bog-function arising from
389 the transmissivity (c) and water level functions (d), which transforms the Poisson “elevation”
390 ϕ **(f)** to peat surface elevation p **(g)**. This bog-function is intermediate between models of
391 Ivanov / Ingram (square-root bog-function) and Cobb et al. (2017) (linear bog-function).

392 **Fig. 4. Estimating whole-bog morphology and irrecoverable carbon stocks from a single**
393 **elevation transect.** **(a)** Reksuo, a raised bog in Finland. Satellite image: Google, Landsat /
394 Copernicus. **(b)** Lidar-derived elevations from the bog boundary and a transect provide a
395 sample of the bog-function describing the relationship between the solution to Poisson’s
396 equation $\phi(x,y)$ and surface elevations p . By transforming the solution to Poisson’s equation
397 **(c)** using this approximate relationship **(d)**, the bog morphology can be estimated with high
398 accuracy in unsurveyed parts of the bog **(e vs. f)**; root-mean-squared error 18.5 cm, bias -0.81
399 cm). Subtracting a horizon that represents the limit of drainability using a grid of ditches **(g**;
400 Methods) from the inferred morphology yields a map of the drainable thickness of peat **(h)**,
401 which closely matches estimates based on the complete surface morphology from lidar **(i)**. **(j)**
402 Cross-section along transect in (a), showing peat surface from the lidar transect (b, blue dots),
403 approximate surface from bog-function (d, black line), drainability horizon (g), and the

404 underlying clay substrate.⁵⁷ **(k)** Vulnerable carbon stock in gigagrams (Gg) of each bog
405 shown in Figs. 1 and 4 and Extended Data Fig. 1 based on its shape inferred from an
406 elevation transect (a–i), vs. vulnerable carbon stock computed from its lidar-measured
407 volume.

408 **Methods**

409 We first discuss the conditions that cause raised bog morphology to be rank-correlated
410 with a solution to Poisson's equation. We show that under these conditions a change of
411 variables transforms nonlinear equations for the shape of the average water table and peat
412 surface into Poisson's equation. We then show how this approach can be used to estimate the
413 morphology and the irrecoverable carbon stored by bogs around the world. Finally, we
414 describe how we obtained lidar-based digital terrain maps and tested our approach.

415 **Observations underlying the bog-function approach**

416 We begin from four observations about raised bogs:

417 *Observation 1.* The water table resides near the surface everywhere in a bog²⁰, because where
418 it does not, peat tends to accumulate or decompose towards an elevation near the mean water
419 table.⁷ Where the water level—defined as the elevation of the water table minus the elevation
420 of the peat surface—is higher, peat is protected from oxidation, and accumulates. Where the
421 water level is lower, peat is exposed and decomposes.¹⁹

422 *Observation 2.* Water levels at different locations across a bog move up and down in a similar
423 way, so that the overall shape of the water table remains nearly steady as it is shifted up and
424 down by rainfall, groundwater flow and evapotranspiration^{4,41,58,59}.

425 *Observation 3.* Peat structure and hydraulic properties show steep gradients in vertical
426 profile⁶⁰ but average properties vary little over horizontal distances of tens to hundreds of
427 metres^{4,40-42}.

428 *Observation 4.* To the extent that water level and hydraulic properties vary, they both tend to
429 have weak trends with distance from the bog margin⁶¹, possibly linked to an ecotone at the
430 bog margin (the lagg²⁰) or concentric zones of plant communities^{18,62,63}, and are thus
431 correlated with peat surface elevation.

432 **Assumptions based on observations**

433 From these general observations we reach the following four assumptions, which we use
434 to derive an equation that implicitly describes bog morphology:

435 *Assumption 1.* The water table elevation increases monotonically with peat surface elevation,
436 i.e., where the peat surface elevation p is higher, the water table H is higher and vice versa,
437 based on observations 1 and 2.

438 *Assumption 2.* The water table gradient at any location is approximately constant with time,
439 as implied by observation 2. Because the water table moves up and down uniformly, its
440 gradient remains approximately the same, and equal to the gradient of the time-averaged
441 water table.

442 *Assumption 3.* Transmissivity, or the depth-integrated flow rate produced by a given water
443 table gradient, is a function of the peat surface elevation p and the water level relative to the
444 surface $H - p$. This assumption generalizes approximations commonly used in peatland
445 hydrology that transmissivity is a function of water level and / or peat thickness above a flat
446 substrate),^{4,6,7,41} while allowing for weak spatial trends in hydraulic properties correlated with
447 peat surface elevation (observations 3 and 4).

448 *Assumption 4.* Average net precipitation (precipitation P minus evapotranspiration ET) is
449 spatially uniform.

450 **Change-of-variables linking bog morphology to Poisson's equation**

451 We now demonstrate that a change of variables, under the assumptions above, links the
452 water table and bog morphology to Poisson's equation. We are interested in time-averaged
453 behaviour over years, the timescales over which bog morphology develops. Therefore, we
454 derive results for time-averages, denoted by angle brackets $\langle \rangle$, on a fixed time interval over
455 which net precipitation is nonzero, and net changes in water storage and the peat surface
456 elevation are small; to simplify our explanation, we consider the averaging interval to be a

457 year. We start from Boussinesq's equation for approximately horizontal groundwater flow

458

$$459 \quad S_y \frac{\partial H}{\partial t} = P - ET + \nabla \cdot (T \nabla H),$$

460 which describes the rise or fall of the water table H (elevation above sea level) in response to

461 net precipitation $P - ET$ and the divergence of groundwater flow $\nabla \cdot (T \nabla H)$. This equation is

462 strongly nonlinear⁴¹ because the depth-integrated groundwater flow $T \nabla H$ is controlled by the

463 transmissivity T , and the transmissivity $T(H, p)$ is itself a function of the water level and the

464 peat surface elevation (assumption 3). Based on approximate water balance $\langle S_y \partial H / \partial t \rangle = 0$,

465 the year's net precipitation is balanced by the time-averaged divergence of horizontal flow

$$466 \quad -\langle P - ET \rangle = \nabla \cdot \langle T \nabla H \rangle.$$

467 When water table fluctuations are uniform (assumption 2), the instantaneous gradient in the

468 water table is equal to its time average $\nabla H(t) = \nabla \langle H \rangle$, and thus the average horizontal flow

469 $\langle T \nabla H \rangle$ anywhere in the peatland is equal to the average water table gradient $\nabla \langle H \rangle$ times the

470 average transmissivity at that location, $\langle T \nabla H \rangle = \langle T \rangle \nabla \langle H \rangle$, yielding

$$471 \quad -\langle P - ET \rangle = \nabla \cdot [\langle T \rangle \nabla \langle H \rangle]. \quad (1)$$

472 Note that although average net precipitation $\langle P - ET \rangle$ is spatially uniform

473 (assumption 4), the average water table $\langle H \rangle(x,y)$ and hence the average transmissivity $\langle T \rangle(x,y)$

474 vary across the bog. Also, the time-averaged transmissivity $\langle T \rangle(x,y)$ is not generally equal to

475 the transmissivity at the average water table $T(\langle H \rangle(x,y), p(x,y))$ because transmissivity is

476 typically a strongly nonlinear function of the water level.⁴¹ Therefore, it is difficult to gain

477 general insights from equation (1). However, as we will now show, because of the special

478 characteristics of bogs (assumptions 1–4) the average transmissivity $\langle T \rangle$ can be written as a

479 function of the average water table $\langle H \rangle$ and therefore it is possible to transform this nonlinear

480 equation (1) into Poisson's equation, enabling our general analysis.

481 To proceed, we first show that under assumptions 1 and 3 the time averaged
482 transmissivity $\langle T \rangle$ at any location is uniquely determined by the time averaged water table
483 $\langle H \rangle$ there. By assumption 1, the water table H increases monotonically with the peat surface
484 elevation p . Consequently, any two distinct surface elevations p correspond at any time to
485 two distinct water table elevations H , and two distinct annual average water table elevations
486 $\langle H \rangle$. By assumption 3, transmissivity T is determined by the surface elevation p and the water
487 level $H - p$, but the water table elevation H at any time is uniquely identified by the surface
488 elevation and therefore the surface elevation p also identifies the transmissivity T . Because
489 the average water table $\langle H \rangle$ identifies the surface elevation p , and the surface elevation p
490 identifies the instantaneous transmissivity, it follows that, in a given year, the average
491 water table $\langle H \rangle$ at a location also uniquely identifies the time-averaged transmissivity there
492 $\langle T \rangle$. Therefore we can define a function f (specific to the year) that transforms the average
493 water table elevation at any location in the bog to the average transmissivity

$$494 \quad \quad \quad \langle T \rangle(x, y) = f[\langle H \rangle(x, y)](P - ET) \quad (2)$$

495
496
497 where we have normalised by net precipitation, which is spatially uniform by assumption 4.
498 This normalisation reduces the effect of the averaging interval on f (see Example with
499 dynamic water tables, below). Substituting this equation (2) for time-averaged transmissivity
500 $\langle T \rangle$ into the time-averaged water balance equation (1) and cancelling net precipitation, we
501 have

$$502 \quad \quad \quad -1 = \nabla \cdot [f(\langle H \rangle)\nabla\langle H \rangle]. \quad (3)$$

503 If we could define a scalar field $\phi(x, y)$ that had a gradient proportional to the contents of the
504 brackets $[\]$ in this equation (3), we would have Poisson's equation.

505 We now define the Poisson "elevation" ϕ as the integral of the function f in equation
506 (2)

507
$$\phi = k \int_{z=0}^{\langle H \rangle} f(z) dz \quad (4)$$

508 scaled by a constant k chosen to make ϕ dimensionless. Taking the gradient of equation (4)
509 and applying the fundamental theorem of calculus gives $\nabla\phi = k[f(\langle H \rangle)\nabla\langle H \rangle]$. Substituting this
510 result for the square brackets $[\]$ in equation (3), and using the definition of the Laplacian
511 operator $\nabla^2 = \nabla \cdot \nabla$, equation (1) for the average water table can be expressed equivalently as
512 Poisson's equation in the Poisson "elevation" ϕ

513
$$-\nabla^2\phi = k. \quad (5)$$

514 This Poisson "elevation" ϕ is convertible to the surface elevation p through a two-step
515 transformation. Inverting equation (4) transforms the Poisson elevation $\phi(x,y)$ to the mean
516 water table $\langle H \rangle(x,y)$ (the function is invertible because transmissivity is strictly positive); and
517 the mean water table elevation $\langle H \rangle$ determines the peat surface elevation $p(x,y)$ because the
518 peat surface elevation is monotonically related to the mean water table elevation (assumption
519 1). The bog-function $p(\phi)$, which converts Poisson "elevations" ϕ to actual bog surface
520 elevations p , is the composition of these two transformations. An example of the two-step
521 process is given below (Example: Hybrid between existing steady-state models); a later
522 section (Solving Poisson's equation and determining the bog-function) describes how we
523 determined bog-functions empirically for the bogs in Fig. 1.

524 The constant k can be thought of as a representative curvature for raised bogs, divided
525 by a reference height scale. In our analysis, we took a perfectly round 1 km² bog with a mean
526 thickness of 1 m and uniform curvature as our reference⁶⁴, giving $k = 8\pi \text{ km}^{-2}$. Using a
527 universal value for the constant k allows us to see how the potential for peat accumulation is
528 controlled by the size and shape of the bog boundary across sites (Fig. 1e).

529 **The bog-function $p(\phi)$**

530 The bog-function $p(\phi)$ and the dimensionless Poisson “elevation” ϕ describe different
531 aspects of a bog’s morphology. The dimensionless Poisson “elevation” ϕ represents an
532 abstract reference morphology implied by the geometry of the bog boundary, independent of
533 climate and ecosystem. In contrast, the bog-function $p(\phi)$, which produces the peat surface
534 morphology $p(x,y)$ from the Poisson “elevation” (Fig. 1), encapsulates the ecosystem
535 processes that determine how the average transmissivity, normalised by net precipitation,
536 varies with mean water table elevation in a particular bog in a specific climate regime. A
537 steeper bog-function can be expected under conditions that are known to favour bog
538 convexity, including an older bog, a wetter climate, faster organic matter production, and
539 slower decomposition,^{3,4,6,7} though a full exploration of the effects of these factors on the
540 bog-function awaits further study.

541 The bog-function is approximately constant across year-to-year climate variability
542 because the peat surface is quasi-steady and the solution to the Poisson equation (3) is
543 uniquely determined by its boundary conditions. Although the functions $f(\langle H \rangle)$ and $\phi(\langle H \rangle)$
544 that relate the mean water table to the mean transmissivity and Poisson “elevation” may vary
545 from year to year and may also be infeasible to measure or compute, whenever our
546 assumptions (1–4) are satisfied, these functions exist, and the relationship between Poisson
547 “elevation” ϕ and surface elevation p holds (see also Example with dynamic water tables,
548 below).

549 **Link between the Poisson “elevation” ϕ and the Girinsky potential**

550 Similar changes of variables are a standard strategy for solving nonlinear variants of
551 Poisson’s equation like equation (1)^{65,66}. A related change-of-variables has been used to
552 derive the shape of the water table in groundwater flow problems, using a variable called the
553 Girinsky potential^{67,68}. The Girinsky potential is written as the integral of hydraulic
554 conductivity K weighted by depth below the water table

555
$$\Gamma = \int_{z=0}^H (H - z)K(z)dz.$$

556 Because the integral of conductivity with respect to depth is the transmissivity $T =$

557 $\int_{z=0}^H K(z) dz$, the Girinsky potential can also be written as an integral of the transmissivity:

558 splitting terms and integrating by parts,

559
$$\Gamma = H \int_{z=0}^H K dz - \int_{z=0}^H z K dz = HT - [zT]_{z=0}^H + \int_{H'=0}^H T(H') dH' = \int_{H'=0}^H T(H') dH'.$$

560 Thus, the Poisson “elevation” ϕ defined here is similar to the Girinsky potential, with the

561 addition of time-averaging to cope with fluctuating water tables (equation 1) and

562 normalisation by the constant k and net precipitation (equations 2–4).

563 **Example: Uniform conductivity, steady-state model of Ivanov**

564 As an example, we consider the case of steady flow through peat with a uniform

565 conductivity above an impermeable substrate at the drainage elevation, discussed in one

566 dimension by Ivanov⁴ and Ingram⁶ and since applied widely, with varying results⁶⁹. If the

567 uniform conductivity model is extended above the minimum water table, it implies large,

568 non-uniform water table fluctuations, which are not observed. Ivanov and Ingram did not

569 consider water table fluctuations with rainfall in their derivation and we assume that they

570 envisioned such fluctuations being suppressed by a highly permeable layer near the peat

571 surface or by overland flow. If steady flow occurs through peat with uniform conductivity,

572 the transmissivity $T = KH$ is the product of the conductivity K and the water table elevation

573 above the substrate H , leading to a steady-state water table equation

574
$$P - ET = -\nabla \cdot (KH \nabla H).$$

575 Defining $\phi = k \int_{z=0}^H z dz = H^2 / (P - ET)$ with $k = 2 / K$ for this example and substituting, we

576 obtain Poisson’s equation (3), or, rearranging,

$$\frac{2(P - ET)}{K} = -\nabla^2 H^2.$$

577

578 By solving Poisson's equation and taking the square root of the result, we obtain the steady
 579 water table elevation. If, as assumed by Ivanov⁴ and Ingram⁶, the water level relative to the
 580 surface ζ (water table minus surface elevation, $\zeta = H - p$) is uniform, the peat surface
 581 elevation is obtained easily from the water table as $p = H - \zeta$.

582 **Example: Hybrid between existing steady-state models**

583 For the hybrid example shown in Fig. 3, we extended the above simple uniform-
 584 conductivity model as follows. We first chose a linear function for time-averaged
 585 transmissivity $\langle T \rangle$ vs. time-averaged water table $\langle H \rangle$

$$586 \quad \langle T \rangle = T_o + K \langle H \rangle, \quad (6)$$

587 which is a generalisation of the steady-state uniform-conductivity model of Ivanov⁴ and
 588 Ingram⁶ and the stationary uniform-transmissivity model of Cobb et al.⁷. This equation (6) is
 589 a specific instance of equation (2) for time-averaged transmissivity $\langle T \rangle$ as a function of time-
 590 averaged water table elevation $\langle H \rangle$. We then chose a function for the mean water level
 591 $\langle \zeta \rangle$ relative to the peat surface in terms of the water table elevation

$$592 \quad \langle \zeta \rangle = \zeta_o + c \langle H \rangle$$

593 and set its parameters arbitrarily to $\zeta_o = -0.1$ m and $c = 0.005$.

594 Recalling that peat surface elevation $p = \langle H \rangle - \langle \zeta \rangle$, we integrated equation (2) to
 595 compute the Poisson "elevation"

$$596 \quad \phi = \frac{1}{b} \left[\langle H \rangle T_o + \frac{1}{2} K \langle H \rangle^2 \right]$$

597 where $b = (P - ET)/k$. By solving the quadratic, we then recovered the mean water table
 598 elevation $\langle H \rangle$ with non-zero catotelm conductivity $K \neq 0$ as

599
$$\langle H \rangle = \frac{1}{K} \left(\sqrt{T_o^2 + 2Kb\phi} - T_o \right)$$

600 or, for negligible catotelm conductivity $K = 0$, $\langle H \rangle = b\phi / T_o$. The smooth or ideal surface p
 601 is obtained easily from the mean water table elevation $\langle H \rangle$ as

602
$$p = (1 + c)\langle H \rangle - \zeta_o$$

603 and thence the simulated surface \tilde{p} is obtained by adding noise ε

604
$$\tilde{p} = p + \varepsilon(x, y).$$

605 **Example with dynamic water tables**

606 To illustrate how this simple approximation for the quasi-steady form of the peat surface
 607 and average water table is compatible with highly dynamic water tables, we re-analysed a
 608 flowtube simulation of water table dynamics in the Mendaram bog presented in ref.⁷
 609 (Extended Data Fig. 2). The simulation models the 3000-year development of the Mendaram
 610 bog using a flowtube hydrological and peat accumulation model; in this analysis, we examine
 611 the portion of the simulation in the recent past, when the simulation closely approximates the
 612 modern peat surface as determined by lidar⁷. The simulation satisfies the assumptions behind
 613 our approach, because flow is driven by uniform net precipitation and the flow domain is a
 614 one-dimensional flowtube bounded by fixed flowlines (Extended Data Fig. 2a), so there is,
 615 trivially, a unique water table height H for each distinct surface elevation p ; and the
 616 transmissivity T in the simulation is a function of the water level ζ .

617 As the example demonstrates, with varying rainfall, the dynamics of the water table and
 618 their instantaneous effect on transmissivity may be complex. Simulated water level
 619 fluctuations in the bog margin and interior are similar (Extended Data Fig. 2b), but subtly
 620 different, leading to higher mean water levels in the bog interior (Extended Data Figs. 2c and
 621 d). In these simulations, transmissivity is a strongly nonlinear function of the water level
 622 (Extended Data Fig. 2e), so that differing distributions of water level across years and

623 locations lead to different mean transmissivities, even at the same mean water level
624 (Extended Data Fig. 2f).

625 Nonetheless, the fundamental constraint imposed by approximate water balance over
626 annual time scales leads to a monotonic and stable relationship between peat surface
627 elevation and the Poisson “elevation” ϕ . Because mean water table gradients are similar from
628 year to year, and changes in net storage over each year are small, most of the variation in net
629 precipitation across years must be compensated by changes in mean transmissivity (equation
630 (1)). Thus, mean transmissivity normalised by net recharge is essentially independent of the
631 year considered (Extended Data Fig. 2g). Minor inter-annual differences in the function f
632 relating mean water table elevation to recharge-normalised transmissivity are compensated by
633 changes in mean water level $\langle \zeta \rangle$, so that the bog-function $p(\phi)$ is the same across years
634 (Extended Data Fig. 2h). This compatibility with highly dynamic water tables enables the
635 application of the bog-function approach to real bogs from all climate settings without
636 permafrost, from northern to tropical to southern latitudes.

637 **Digital terrain models from lidar data**

638 We derived digital terrain models (DTMs) from lidar data for each of the eight bogs we
639 analysed, at Hamilton Bay (Alaska, USA), Milot (Quebec, Canada), Great Cranberry Island
640 (Maine, USA), Valgeraba (Estonia), Mendaram (Brunei Darussalam), Kopuatai (New
641 Zealand), Reksuo (Finland), and Lost River (Minnesota, USA). For Valgeraba and Milot, we
642 downloaded freely available lidar-derived DTMs provided by the Estonian Topographic
643 Database (10 m resolution; <https://geoportaal.maaamet.ee/>) and the Natural Resources of
644 Canada HRDEM project (1 m resolution; <http://open.canada.ca/en/open-maps>). For the other
645 six sites, we obtained lidar point cloud data from these portals: Hamilton Bay: USGS
646 National Map, product LPC AK POW P2 2018 (<https://nationalmap.gov>); Lost River:
647 Minnesota Geospatial Information Office (<https://www.mngeo.state.mn.us/>); Great Cranberry

648 Island: USGS National Map, product LPC ARRA-LFTNE MAINE 2010
649 (<https://nationalmap.gov>); Reksuo: National Land Survey of Finland
650 (<https://tiedostopalvelu.maanmittauslaitos.fi/tp/kartta?lang=en>); Mendaram: Brunei
651 Darussalam Survey Department (purchased; <https://survey.gov.bn>); Kopuatai:
652 OpenTopography (collection Huntly, Waikato, New Zealand 2015-2019,
653 <https://portal.opentopography.org>).

654 For Valgeraba and Milot, we downsampled the available 10 m and 1 m lidar-derived
655 DTMs to a 20 m resolution DTM using a geospatial translator library⁷⁰. For Hamilton Bay,
656 Lost River, Great Cranberry Island, Reksuo, Mendaram, and Kopuatai, we created DTMs
657 from the lidar data as follows. We first filtered point cloud data to last-return points (using
658 libLAS version 1.8.1, <http://liblas.org>, and PDAL version 2.4.3, <https://pdal.io/>). We then
659 removed outliers among last-return points using two methods: (1) within each cell of a
660 Cartesian grid, we removed outliers more than 3 times the interquartile range below the lower
661 quartile (Tukey's fence) and recorded the value and location of the lowest among the
662 remaining points; and (2) we removed points with deviations of more than 2 m (Hamilton
663 Bay) or 3 m (all other sites) from a bicubic spline surface through the points [using
664 `v.outlier`⁷¹]. Note that this surface was used only to identify outliers, and not to create the
665 elevation rasters. The remaining local minima were used to construct a gridded DTM for each
666 of these sites by inverse-distance weighted interpolation using a geospatial translator
667 library⁷⁰. The Cartesian grid sizes used for the sites were 10 m for Hamilton Bay and Milot;
668 20 m for Great Cranberry Island, Reksuo, Valgeraba, and Mendaram; and 30 m for Lost
669 River and Kopuatai.

670 These unsmoothed elevation rasters were used for all calculations except for drawing
671 flowlines (Figs. 1, 4 and Extended Data Fig. 1), for which local minima in the raw elevation
672 rasters sometimes prevented assembly of complete flowlines. For drawing flowlines in

673 figures, and for this purpose only, we gridded lidar-derived points using inverse-distance
674 weighted interpolation with smoothing (using `gdal_grid`⁷⁰).

675 **Drawing bog boundaries**

676 We drew a boundary for each bog with a Geographic Information System (QGIS,
677 <https://qgis.org>), using visual imagery (Google Tile Map Service) to identify bog edges based
678 on shifts in vegetation and with reference to maps and descriptions in literature sources for
679 Hamilton Bay⁷², Lost River⁷³, Milot⁷⁴, Great Cranberry Island⁷⁵, Reksuo⁷⁶, Valgeraba^{77,78},
680 Mendaram⁷⁹, and Kopuatai^{80–83}. Because the extended Poisson equation (5) is satisfied in any
681 portion of a bog where assumptions 1–4 are valid (see Assumptions based on observations),
682 the bog-function approach does not require that a bog is bounded by channels (cf. refs.^{6,7}).
683 Thus, our approach is applicable to bogs embedded in large peatland complexes, such as
684 those covering thousands to millions of hectares in areas of North America, Peru, Ireland,
685 Scandinavia, and Siberia^{62,84–87}, where water may flow out of a bog into marginal fens, or
686 may discharge into mineral soils without breaching the surface^{62,84}. Indeed, one can draw a
687 boundary along any closed curve inside the bog, and solve the Poisson equation inside that
688 curve as if it were the boundary of the bog. This feature made our approach applicable at
689 Hamilton Bay, Lost River, Milot, and Reksuo, where we drew boundaries to exclude patches
690 and fringes of dense vegetation that could reduce the accuracy of lidar ground elevations.

691 Lost River and Kopuatai are both mire complexes with multiple raised bogs. At Lost
692 River, we chose the largest raised bog in the complex because we expected that it would have
693 the highest relief, and thus the greatest signal-to-noise ratio relative to error in the lidar data.
694 The Lost River area was ditched in the early 20th century^{88,89}, and we drew the boundary to
695 exclude an east-west ditch north of the bog crest. In addition, we drew a second boundary
696 ignoring the ditch to show the effects on our analysis if its assumptions are not well satisfied
697 (top row of Extended Data Fig. 1). At Kopuatai, we drew a boundary around the raised bog in

698 the northern part of the mire complex, as it appeared less affected by lidar artefacts from
699 dense vegetation, as discussed later (see Comparing measured and modelled bog
700 morphologies).

701 At two bogs, Milot and Mendaram, elevation data coverage of the bog area was
702 incomplete. In these cases, we adjusted the boundary conditions to use the available data
703 (Extended Data Fig. 3). At Milot, elevation data were unavailable for the south-eastern corner
704 of the bog (Extended Data Fig. 3a). Because the edge of available data lay close to the bog
705 margin, we drew the boundary to exclude the area of missing data and applied fixed-elevation
706 (Dirichlet) boundary conditions. At Mendaram, the available data end at a national border,
707 which passes near the dome crest. In this case, we estimated the location of the bog crest
708 based on the topographic setting of the bog on an interfluvium between two rivers (Extended
709 Data Fig. 3b) and drew a no-throughflow (Neumann) boundary comprising the groundwater
710 divide and estimated flowlines extending to the Agas and Pendaruan Rivers (Extended Data
711 Fig. 3b–d); these rivers are obscured by floating vegetation but are visible in high-resolution
712 images (Extended Data Fig. 3c).

713 **Solving Poisson's equation and determining the bog-function**

714 Provided our assumptions are satisfied, there is a bog-function $p(\phi)$ that relates the bog
715 surface morphology $p(x,y)$ to the solution to Poisson's equation $\phi(x,y)$. Although our analysis
716 begins with known surface elevations p along the boundary, solving Poisson's equation
717 requires the specification of boundary conditions in terms of ϕ . Therefore, in general, the
718 solution of Poisson's equation $\phi(x,y)$ and the determination of the bog-function $p(\phi)$ must be
719 done together.

720 To jointly approximate the solution to Poisson's equation $\phi(x,y)$ and the bog-function
721 $p(\phi)$, we used a simple linear correction to accommodate non-flat boundaries, as we explain
722 now. Suppose that the bog morphology is described by a linear bog-function $p = m\phi + b$ up to

723 some elevation contour p_* which lies above the highest point on the boundary. Then on the
724 part of the bog with surface elevations below p_* , the surface elevation $p(x,y)$ itself satisfies
725 Poisson's equation, like $\phi(x,y)$, but with a different right-hand-side $-\nabla^2 p = mk$. We
726 decompose the surface elevations below p_* into two components $p = p_0 + p_\ell$, where p_0 is
727 the solution to the Poisson equation $-\nabla^2 p_0 = mk$ with a zero boundary, and p_ℓ is the
728 solution to the Poisson equation with the actual boundary elevations and a zero right-hand-
729 side $-\nabla^2 p_\ell = 0$. (On the boundary, $p_0 = 0$ so $p = p_\ell$; and on the interior, $\nabla^2 p_\ell = 0$ so
730 $-\nabla^2 p = -\nabla^2 p_0 = mk$, as required.) We have the boundary elevations, so we can solve the
731 Poisson equation with zero right-hand-side to obtain p_ℓ , and then obtain values for $p_0 = p -$
732 p_ℓ by subtraction. But in the part of the bog where $p \leq p_*$, p_0 also satisfies the Poisson
733 equation $-\nabla^2 p_0 = mk$ with a zero boundary. Therefore, if we define a variable ϕ_0 that
734 solves the Poisson equation $-\nabla^2 \phi_0 = k$ with a zero boundary, we can obtain estimates of m
735 and b by linear regression of p_0 against ϕ_0 . We can then use the linear approximation $p \approx m\phi$
736 $+ b$ to convert the elevations p into values for ϕ on the boundary, and solve for Poisson
737 "elevations" $\phi(x,y)$ in the interior.

738 To apply this strategy and obtain the solution to Poisson's equation $\phi(x,y)$ and the bog-
739 function $p(\phi)$, we first numerically solved Poisson's equation $-\nabla^2 \phi_0 = k$ with zero boundary
740 conditions as described in ref.⁶⁴. Briefly, we created a quadrilateral mesh within each
741 boundary⁹⁰ and solved Poisson's equation on the mesh with a solver written in Cython
742 (<http://cython.org>) using a finite element library (deal.II^{91,92}). We sampled the numerical
743 solution for each mesh (using VTK Python, <http://vtk.org>) on a grid matching that of the
744 bog's lidar-derived elevation raster. We then solved the Poisson equation again with zero
745 right-hand-side and boundary elevations from the DTM to obtain p_ℓ . We set a threshold peat
746 surface elevation p_* to at least the highest boundary elevation, but no less than 60 cm above
747 the lowest point on the boundary, to ensure stable regression results given noise in the DTM

748 data. We then extracted all surface elevations below this threshold and obtained the slope m
749 of the bog-function near the boundary as the slope of $p - p_\ell$ against ϕ_0 , and set the arbitrary
750 offset b so that $\phi = 0$ at the average elevation of p_ℓ . We used these regression coefficients m ,
751 b for the sole purpose of obtaining boundary conditions in terms of ϕ , and then solved
752 Poisson's equation for $\phi(x,y)$ in the bog interior.

753 We next obtained the bog-function $p(\phi)$ for the entire bog using rank regression.⁹³
754 Regression of ranks $R(p)$ of surface elevations against ranks $R(\phi)$ of Poisson "elevations"
755 yielded a slope m_r and intercept b_r , which we used to compute estimated ranks $\hat{R}(\hat{p})$ of
756 surface elevation from ranks $R(\phi)$ of Poisson "elevation"

$$757 \quad \hat{R}(\hat{p}) = m_r \hat{R}(\hat{\phi}) + b_r.$$

758 The estimated surface elevation \hat{p} was then determined from its estimated rank $\hat{R}(\hat{p})$ by
759 linear interpolation. The resulting function $\hat{p}(\phi)$ is guaranteed to be non-decreasing because
760 of the properties of rank regression and therefore satisfies the requirements of a bog-function,
761 and plotting $\hat{p}(x, y)$ in space produces a morphology that represents the approximation
762 resulting from our assumptions.

763 We note that this strategy for estimating the bog-function does not attempt to optimize
764 the mean-squared error in the Poisson-derived morphology relative to the measured
765 morphology, and therefore we believe that even better strategies could be devised. However,
766 this strategy has the advantages of being simple and noniterative, and yields excellent results
767 in practice (Figs. 1 and 4, Extended Data Fig. 1).

768 **Comparing measured and modelled bog morphologies**

769 To evaluate rank-correlation between the solution to Poisson's equation $\phi(x,y)$ and
770 lidar-determined DTM elevations $p(x,y)$, we computed Spearman's rank correlation
771 coefficient ρ as the correlation between the ranks $R(\phi)$ of Poisson "elevations" and the ranks
772 $R(p)$ of the surface elevations. To evaluate the accuracy of Poisson-derived morphologies,

773 we computed root-mean-squared differences between lidar and Poisson-derived
774 morphologies as the square-root of the sum of squared differences between elevations in each
775 pixel of the lidar and Poisson-derived elevation rasters. We also computed the coefficient of
776 determination R^2 of the Poisson-derived morphologies in the standard way, as one minus the
777 sum of squared differences divided by the variance in lidar raster elevations.

778 Whereas Spearman's rank correlation coefficient ρ quantifies the monotonicity of the
779 relationship between the Poisson- and lidar-derived elevations, the coefficient of
780 determination R^2 quantifies the agreement between our approximation and the lidar surface,
781 with its accompanying measurement error. Vertical accuracy of lidar DTMs in different
782 biomes ranges from 12 cm to 195 cm RMSE⁹⁴. In addition, the hummock-and-hollow surface
783 patterning typical of peatlands creates local variation in surface elevation, not modelled by
784 our theory, of up to 50 cm over distances of a few metres^{7,31,95}.

785 The largest source of error in lidar DTMs in non-mountainous habitats is dense foliage
786 that prevents the beam from hitting the ground⁹⁴. The areas most affected by such errors
787 appeared to be dense conifer stands and patches in northern bogs, and patches in the restiad
788 bogs at Kopuatai, where interlocking restiad stems can block light penetration⁹⁶. Conifers in
789 northern bogs were mostly found in the lagg ecotone at the bog edge, and were avoided by
790 drawing the boundary accordingly. At Lost River and Kopuatai, patches of conifers and
791 restiads, respectively, occurred within the bog expanse and could not be excluded; their
792 effects are visible in the lidar DTMs (Fig. 1 and Extended Data Fig. 1) and help to explain the
793 lower correlation coefficients for those two bogs.

794 **Estimating overall bog morphology from an elevation transect**

795 We computed transect-derived morphologies in the same way as the Poisson-derived
796 morphologies, except that the bog-function for transforming Poisson elevations ϕ to
797 estimated elevations \hat{p} was created using only lidar and Poisson elevations within 30 m of

798 the transect, selected using a spatial database (PostGIS, <https://postgis.net/>). The transects
799 were drawn through the bog crest to span the range of elevations in the bog and to illustrate
800 the complexity of elevation profiles that can arise with natural bog boundaries.

801 **Estimating irrecoverable carbon in bogs**

802 Because current interest in peatland carbon stocks is motivated by their potential climate
803 impact following drainage,^{12,13,19,26,29,30} we estimated the carbon in each bog that is vulnerable
804 to emission as carbon dioxide upon land-use conversion, following the definition of
805 irrecoverable carbon in refs.^{30,43}. Modern land-use conversion of a raised peatland typically
806 starts with removal of trees and excavation of a uniform rectangular grid of ditches or
807 subsurface drains discharging at the bog boundary.^{8,20,27,44–46} As carbon is lost to aerobic
808 decomposition and fire and the peat surface subsides, ditches are deepened,^{20,47} until peat is
809 no longer drainable by this approach. At the limit of drainability, the peat surface will no
810 longer be raised and will resemble the solution to Laplace's equation (e.g., Fig. 4g), which
811 can be pictured as an elastic sheet stretched across the bog boundary. Peat below this surface
812 is only drainable by careful exploitation of site-specific conditions,^{97,98} by pumping,²⁷ or the
813 creation of polders, which is rarely done for new land conversion because it is complex,
814 expensive, and, in areas of high rainfall, infeasible.^{27,46,99,100} We therefore estimated each
815 bog's irrecoverable carbon stock as the volume of peat above this drainability horizon
816 multiplied by an appropriate carbon density (see Carbon density, below). To calculate the
817 drainability horizon for each bog, we drew a second polygon at the edge of the raised part of
818 the bog, which in some cases lay outside the boundary used for estimating the bog
819 morphology (see notes under Drawing bog boundaries, above). The calculated drainability
820 horizons for all bogs are included in the linked dataset.¹⁰¹

821 Although our focus is on irrecoverable carbon stocks, that is, vulnerable carbon stocks
822 directly relevant to climate action,³⁰ we note that our approach can be combined with a

823 sample of peat thicknesses to estimate total carbon stocks in raised bogs, including both
824 vulnerable and safe pools. Though the safe carbon pool in bogs is not at risk of release in
825 typical modern land-use change events, it is still useful to quantify this safe stock as a part of
826 the biogeochemical cycle of carbon on longer time scales, just as it is valuable to quantify
827 carbon in peats that are now submerged on continental shelves^{102,103} or buried under mineral
828 soils.³⁶ Safe bog carbon is related to bog morphology through a correlation between peat
829 surface elevation and peat thickness observed within many bogs around the world.⁴⁸ This
830 correlation is attributable to the depositional settings in which bogs form. The largest bog
831 complexes of Southeast Asia, North America, and Siberia formed on emerging coastal plains,
832 prograding deltas, ancient sedimentary deposits, or the abandoned basins of vast glacial lakes,
833 where elevation gradients are very small^{4,32,62,84,85,104–106} (slope of correlation ≈ 1). Smaller,
834 isolated bogs of North America and Europe typically formed in depressions,^{62,84} so that the
835 substrate is concave and the surface is convex⁴⁸ (slope of correlation > 1). In either case, the
836 parameters of the correlation between peat surface elevation and thickness are identifiable
837 from a sample of thicknesses obtained by manual soundings or geophysical methods.^{48,107–109}
838 Combining these parameters with bog morphology then provides an estimate of mean peat
839 thickness; the uncertainty can be made arbitrarily small by taking more soundings. In cases
840 where the correlation is weak, this approach devolves to a full thickness survey, but where
841 the correlation is strong, availability of bog surface morphology will greatly reduce the effort
842 required to estimate safe bog carbon stocks, in addition to vulnerable stocks.

843 To illustrate vulnerable carbon, safe carbon, and the boundary between the two, we
844 plotted a cross-section through Reksuo bog in Finland (Fig. 4j). To show the profile of the
845 underlying clay substrate at Reksuo, we digitized contours of clay subsurface elevations from
846 Fig. 3D of ref. ⁵⁷. For each intersection between a contour and the profile transect (shown in
847 Fig. 4a), we recorded the contour elevation and the distance of the intersection from the end

848 of the transect. These points mark the upper boundary of the clay in the cross-section shown
849 in Fig. 4j.

850 **Carbon density**

851 Estimates of both vulnerable and safely sequestered carbon require site data on the
852 carbon density of the peat in a bog. A carbon density for each site was obtained from peat
853 core data from the bog itself or a nearby bog as follows. For Hamilton Bay, Lost River, and
854 Milot, we used the mean dry bulk density of cores in ref.⁷⁴ from Pleasant Island, Red Lake,
855 and Milot, multiplied by the carbon content of 0.517 used by ref.²³, giving carbon densities of
856 45.7 kg C m⁻³, 46.8 kg C m⁻³, and 38.2 kg C m⁻³, respectively. For Great Cranberry Island,
857 we obtained a carbon density of 50.4 kg C m⁻³ from the mean bulk density and carbon
858 content of the “Sidney Bog” core from Dan Charman in the database of Loisel et al.¹¹⁰. For
859 Reksuo, we used 25.1 kg C m⁻³, computed from mean carbon content to a depth of 549 cm in
860 the Siikaneva core from Paul Mathijssen in the same database¹¹⁰. For Valgeraba, we used
861 44.7 kg C m⁻³, computed from tabulated core data from Nigula Raba given in ref.¹¹¹. For
862 Mendaram, we computed a value of 39.2 kg C m⁻³ from mean dry bulk density and carbon
863 content of a core at that site¹¹². For Kopuatai, we used a value of 25.6 kg C m⁻³ computed
864 from mean bulk density⁸¹ and carbon content¹¹³ of peat samples at the site.

865 **Peatland mean annual temperature and precipitation**

866 To plot the mean annual temperature and precipitation of literature peatland study sites
867 (Fig. 2b), we sampled WorldClim mean annual temperature and mean annual precipitation
868 rasters (WorldClim version 2.1; 30 arc-second grid, 1970–2000⁵⁵) using peatland geographic
869 coordinates provided by ref.³⁶. We added the global land surface to this plot by transforming
870 the WorldClim rasters to an equal-area projection (Mollweide) and shading each hexagonal
871 partition of temperature-precipitation climate space containing at least one land pixel. We

872 obtained mean annual temperature and precipitation for each of the eight bogs analysed here
873 by sampling at the centroid of its boundary from the same WorldClim rasters.

874

875 **Data availability**

876 The lidar and topographic data used in this study are available from the Estonian
877 Topographic Database, the Natural Resources of Canada HRDEM project, USGS National
878 Map (products LPC AK POW P2 2018 and LPC ARRA-LFTNE MAINE 2010), Minnesota
879 Geospatial Information Office, National Land Survey of Finland, the Brunei Darussalam
880 Survey Department, and OpenTopography (collection Huntly, Waikato, New Zealand 2015-
881 2019). The derived data reported in this paper have been deposited in the PANGAEA open
882 access data archive, [doi:10.1594/PANGAEA.931195](https://doi.org/10.1594/PANGAEA.931195).

883 **Methods references**

- 884 58. Edom, F., Münch, A., Dittrich, I., Keßler, K. & Peters, R. Hydromorphological analysis
885 and water balance modelling of ombro- and mesotrophic peatlands. *Advances in*
886 *Geosciences* **27**, 131–137 (2010).
- 887 59. Hooijer, A. Hydrology of tropical wetland forests: Recent research results from Sarawak
888 peatswamps. in *Forests, Water and People in the Humid Tropics* (eds. Bonell, M. &
889 Bruijnzeel, L. A.) 447–461 (Cambridge University Press, Cambridge, UK, 2005).
- 890 60. Rezanezhad, F. et al. Structure of peat soils and implications for water storage, flow and
891 solute transport: A review update for geochemists. *Chemical Geology* **429**, 75–84 (2016).
- 892 61. Baird, A. J., Eades, P. A. & Surridge, B. W. J. The hydraulic structure of a raised bog and
893 its implications for ecohydrological modelling of bog development. *Ecohydrology* **1**,
894 289–298 (2008).
- 895 62. Heinselman, M. L. Forest sites, bog processes, and peatland types in the Glacial Lake
896 Agassiz region, Minnesota. *Ecological Monographs* **33**, 327–374 (1963).
- 897 63. Glaser, P. H. & Janssens, J. A. Raised bogs in eastern North America: Transitions in
898 landforms and gross stratigraphy. *Canadian Journal of Botany* **64**, 395–415 (1986).
- 899 64. Cobb, A. R., Dommain, R., Tan, F., Heng, N. H. E. & Harvey, C. F. Carbon storage
900 capacity of tropical peatlands in natural and artificial drainage networks. *Environmental*
901 *Research Letters* **15**, 114009 (2020).
- 902 65. Press, W. H., Teukolsky, S. A., Vetterling, W. T. & Flannery, B. P. *Numerical Recipes in*
903 *C: The Art of Scientific Computing*. (Cambridge University Press, New York, New York,
904 USA, 2nd ed., 1992).

- 905 66. Averick, B. M. & Ortega, J. M. Fast solution of nonlinear Poisson-type equations. *SIAM*
906 *Journal on Scientific Computing* **14**, 44–48 (1993).
- 907 67. Youngs, E. G. Horizontal seepage through unconfined aquifers with hydraulic
908 conductivity varying with depth. *Journal of Hydrology* **3**, 283–296 (1965).
- 909 68. Youngs, E. G. An examination of computed steady-state water-table heights in
910 unconfined aquifers: Dupuit-Forchheimer estimates and exact analytical results. *Journal*
911 *of Hydrology* **119**, 201–214 (1990).
- 912 69. Belyea, L. R. & Baird, A. J. Beyond ‘The limits to peat bog growth’: Cross-scale
913 feedback in peatland development. *Ecological Monographs* **76**, 299–322 (2006).
- 914 70. GDAL contributors. *GDAL – Geospatial Data Abstraction Library, version 2.3.2*. (Open
915 Source Geospatial Foundation, 2018).
- 916 71. GRASS Development Team. *Geographic Resources Analysis Support System (GRASS*
917 *GIS) software, version 7.4.4*. (Open Source Geospatial Foundation, 2018).
- 918 72. Dachnowski-Stokes, A. P. *Peat Resources in Alaska*. (Technical Bulletin 769, United
919 States Department of Agriculture, Washington, D.C., USA, 1941).
- 920 73. Glaser, P. H., Janssens, J. A. & Siegel, D. I. The response of vegetation to chemical and
921 hydrological gradients in the Lost River peatland, Northern Minnesota. *The Journal of*
922 *Ecology* **78**, 1021 (1990).
- 923 74. Gorham, E., Janssens, J. A. & Glaser, P. H. Rates of peat accumulation during the
924 postglacial period in 32 sites from Alaska to Newfoundland, with special emphasis on
925 northern Minnesota. *Canadian Journal of Botany* **81**, 429–438 (2003).

- 926 75. Raymond, R., Cameron, C. C. & Cohen, A. D. Relationship between peat geochemistry
927 and depositional environments, Cranberry Island, Maine. *International Journal of Coal*
928 *Geology* **8**, 175–187 (1987).
- 929 76. Korhola, A., Alm, J., Tolonen, K., Turunen, J. & Jungner, H. Three-dimensional
930 reconstruction of carbon accumulation and CH₄ emission during nine millennia in a raised
931 mire. *Journal of Quaternary Science* **11**, 161–165 (1996).
- 932 77. Salm, J.-O. et al. Emissions of CO₂, CH₄ and N₂O from undisturbed, drained and mined
933 peatlands in Estonia. *Hydrobiologia* **692**, 41–55 (2012).
- 934 78. Ilomets, M. Estonia. in *Mires and Peatlands of Europe* (eds. Joosten, H., Tanneberger, F.
935 & Moen, A.) 360–371 (Schweizerbart'sche Verlagsbuchhandlung, Stuttgart, Germany,
936 2017).
- 937 79. Anderson, J. A. R. The ecology and forest types of the peat swamp forests of Sarawak
938 and Brunei in relation to their silviculture. (Ph.D. thesis, The University of Edinburgh,
939 1961).
- 940 80. Maggs, G. R. Hydrology of the Kopouatai peat dome. *Journal of Hydrology (NZ)* **36**,
941 147–172 (1997).
- 942 81. Clarkson, B. R., Schipper, L. A. & Lehmann, A. Vegetation and peat characteristics in the
943 development of lowland restiad peat bogs, North Island, New Zealand. *Wetlands* **24**, 133–
944 151 (2004).
- 945 82. Thornburrow, B., Williamson, J. & Outram, P. *Kopuatai Peat Dome Drainage & Desktop*
946 *Hydrological Study: Report Prepared for New Zealand Department of Conservation.*
947 (Sinclair Knight Merz, Auckland, New Zealand, 2009).

- 948 83. Newnham, R. M. et al. Peat humification records from Restionaceae bogs in northern
949 New Zealand as potential indicators of Holocene precipitation, seasonality, and ENSO.
950 *Quaternary Science Reviews* **218**, 378–394 (2019).
- 951 84. Sjörs, H. Bogs and fens in the Hudson Bay Lowlands. *ARCTIC* **12**, 2–19 (1959).
- 952 85. Glaser, P. H., Siegel, D. I., Reeve, A. S. & Chanton, J. P. Hydrogeology of major peat
953 basins in North America. in *Peatlands: Evolution and Records of Environmental and*
954 *Climate Changes* (eds. Martini, T.P., Martinez Cortizas, A., & Chesworth, W.) 347–376
955 (Elsevier, Amsterdam, The Netherlands, 2006).
- 956 86. Vitt, D. H. Functional characteristics and indicators of boreal peatlands. in *Boreal*
957 *Peatland Ecosystems* (eds. Wieder, R. K. & Vitt, D. H.) 9–24 (Springer Berlin
958 Heidelberg, Heidelberg, Germany, 2006).
- 959 87. Honorio Coronado, E. N. et al. Intensive field sampling increases the known extent of
960 carbon-rich Amazonian peatland pole forests. *Environmental Research Letters* **16**,
961 074048 (2021).
- 962 88. Bradof, K. L. Ditching of Red Lake Peatland during the homestead era. in *The Patterned*
963 *Peatlands of Minnesota* (eds. Wright, Jr., H. E., Coffin, B. A. & Aaseng, N. E.) 263–284
964 (University of Minnesota Press, Minneapolis, USA, 1992).
- 965 89. Bradof, K. L. Impact of ditching and road construction on Red Lake Peatland. in *The*
966 *Patterned Peatlands of Minnesota* (eds. Wright, Jr., H. E., Coffin, B. A. & Aaseng, N. E.)
967 173–186 (University of Minnesota Press, Minneapolis, USA, 1992).
- 968 90. Geuzaine, C. & Remacle, J.-F. Gmsh: A 3-D finite element mesh generator with built-in
969 pre- and post-processing facilities. *International Journal for Numerical Methods in*
970 *Engineering* **79**, 1309–1331 (2009).

- 971 91. Bangerth, W., Hartmann, R. & Kanschat, G. Deal.II—A general-purpose object-oriented
972 finite element library. *ACM Transactions on Mathematical Software* **33**, 24/1–24/27
973 (2007).
- 974 92. Arndt, D. et al. The deal.II library, version 9.1. *Journal of Numerical Mathematics* **27**,
975 203–213 (2019).
- 976 93. Iman, R. L. & Conover, W. J. The use of the rank transform in regression. *Technometrics*
977 **21**, 499–509 (1979).
- 978 94. Simpson, J., Smith, T. & Wooster, M. Assessment of errors caused by forest vegetation
979 structure in airborne LiDAR-derived DTMs. *Remote Sensing* **9**, 1101 (2017).
- 980 95. Lampela, M. et al. Ground surface microtopography and vegetation patterns in a tropical
981 peat swamp forest. *Catena* **139**, 127–136 (2016).
- 982 96. Campbell, E. O. Mires of Australasia. in *Mires: Swamp, Bog, Fen and Moor: Regional*
983 *Studies* (ed. Gore, A. J. P.) vol. 4B of *Ecosystems of the world*, 153–180 (Elsevier,
984 Amsterdam, The Netherlands, 1983).
- 985 97. Heathwaite, A. L., Eggelsmann, R. & Göttlich, Kh. Ecohydrology, mire drainage and
986 mire conservation. in *Mires: Process, Exploitation and Conservation* (eds. Heathwaite, A.
987 L. & Göttlich, Kh.) 417–484 (John Wiley & Sons, 1993).
- 988 98. Mulqueen, J. Hydrology and drainage of peatland. *Environmental Geology and Water*
989 *Sciences* **9**, 15–22 (1986).
- 990 99. Joosten, H., Tapio-Biström, M.-L., & Susanna Tol, S., eds. *Peatlands—Guidance for*
991 *Climate Change Mitigation through Conservation, Rehabilitation and Sustainable Use*.
992 vol. 5 (Food and Agriculture Organization of the United Nations and Wetlands
993 International, Rome, Italy, 2nd edition, 2012).

- 994 100. Joosten, H. & Tanneberger, F. Peatland use in Europe. in *Mires and peatlands of*
995 *Europe* (eds. Joosten, H., Tanneberger, F. & Moen, A.) 151–172 (Schweizerbart'sche
996 Verlagsbuchhandlung, Stuttgart, Germany, 2017).
- 997 101. Cobb, A. R., Dommain, R., Yeap, K. & Cao, H. Raster grids of eight bogs in North
998 America, Europe, Borneo, and New Zealand. PANGAEA
999 <https://doi.org/10.1594/PANGAEA.931195> (2023).
- 1000 102. Emery, K. O., Wigley, R. L., Bartlett, A. S., Rubin, M. & Barghoorn, E. S. Freshwater
1001 peat on the continental shelf. *Science* **158**, 1301–1307 (1967).
- 1002 103. Situmorang, M., Kuntoro, Faturachman, A., Ilahude, D. & Siregar, D. A. Distribution
1003 and characteristics of Quaternary peat deposits in eastern Jawa Sea. *Bulletin of the Marine*
1004 *Geological Institute of Indonesia* **8**, 9–20 (1993).
- 1005 104. Kremenetski, K. V. et al. Peatlands of the Western Siberian lowlands: Current
1006 knowledge on zonation, carbon content and Late Quaternary history. *Quaternary Science*
1007 *Reviews* **22**, 703–723 (2003).
- 1008 105. Dommain, R., Couwenberg, J. & Joosten, H. Development and carbon sequestration
1009 of tropical peat domes in south-east Asia: Links to post-glacial sea-level changes and
1010 Holocene climate variability. *Quaternary Science Reviews* **30**, 999–1010 (2011).
- 1011 106. Ruppel, M., Väiliranta, M., Virtanen, T. & Korhola, A. Postglacial spatiotemporal
1012 peatland initiation and lateral expansion dynamics in North America and northern Europe.
1013 *The Holocene* **23**, 1596–1606 (2013).
- 1014 107. Comas, X., Slater, L. & Reeve, A. Geophysical evidence for peat basin morphology
1015 and stratigraphic controls on vegetation observed in a Northern Peatland. *Journal of*
1016 *Hydrology* **295**, 173–184 (2004).

- 1017 108. Comas, X. et al. Imaging tropical peatlands in Indonesia using ground-penetrating
1018 radar (GPR) and electrical resistivity imaging (ERI): Implications for carbon stock
1019 estimates and peat soil characterization. *Biogeosciences* **12**, 2995–3007 (2015).
- 1020 109. Suhip, M. A. A., Gödeke, S. H., Cobb, A. R. & Sukri, R. S. Seismic refraction study,
1021 single well test and physical core analysis of anthropogenic degraded peat at the Badas
1022 Peat Dome, Brunei Darussalam. *Engineering Geology* **273**, 105689 (2020).
- 1023 110. Loisel, J. et al. A database and synthesis of northern peatland soil properties and
1024 Holocene carbon and nitrogen accumulation. *The Holocene* **24**, 1028–1042 (2014).
- 1025 111. Korhola, A., Tolonen, K., Turunen, J. & Jungner, H. Estimating long-term carbon
1026 accumulation rates in boreal peatlands by radiocarbon dating. *Radiocarbon* **37**, 575–584
1027 (1995).
- 1028 112. Dommain, R. et al. Forest dynamics and tip-up pools drive pulses of high carbon
1029 accumulation rates in a tropical peat dome in Borneo (Southeast Asia). *Journal of*
1030 *Geophysical Research: Biogeosciences* **120**, 617–640 (2015).
- 1031 113. Schipper, L. A. & McLeod, M. Subsidence rates and carbon loss in peat soils
1032 following conversion to pasture in the Waikato Region, New Zealand. *Soil Use and*
1033 *Management* **18**, 91–93 (2006).
- 1034

1035 **Acknowledgements**

1036 We are grateful to Joss Ratcliffe for pointing us to lidar data for Kopuatai, and to
1037 Jonathan Cobb, Alex Konings, Joss Ratcliffe, Howard A. Stone, and David Wardle for
1038 critical comments on the manuscript. This research was supported by the National Research
1039 Foundation Singapore through the Singapore-MIT Alliance for Research and Technology’s
1040 Center for Environmental Sensing and Modeling interdisciplinary research program and
1041 Grant Nos. NRF2016-ITCOO1-021 and NRF2019-ITC001-001, by the US National Science
1042 Foundation under Grant No. 1923491, and by the Office for Space Technology and Industry
1043 (OSTIn), Singapore’s national space office, through its Space Technology Development
1044 Programme (Grant No. S22-02005-STDP). This work comprises EOS contribution 552. Lidar
1045 and topographic data were provided by the Estonian Topographic Database, the Natural
1046 Resources of Canada HRDEM project, USGS National Map, Minnesota Geospatial
1047 Information Office, National Land Survey of Finland, Brunei Darussalam Survey
1048 Department, and OpenTopography.
1049

1050 **Author contributions**

1051 A.R.C. conceived the study, performed the analysis, prepared the figures, and drafted
1052 the paper. A.R.C., C.H., K.Y., and R.D. identified and outlined bog sites with lidar data and
1053 developed the workflow for creation of digital terrain maps and meshing of bog polygons.
1054 B.B., C.F.H., and P.H.G. supervised and provided feedback on the study design. A.R.C.,
1055 B.B., C.F.H., N.C.D., and R.D. participated in editing of the final manuscript, and all authors
1056 contributed to review and data interpretation.

1057 **Competing interest declaration**

1058 The authors declare no competing interests.

1059 **Additional information**

1060 **Correspondence and requests for materials** should be addressed to A.R.C.

1061 **Reprints and permissions information** is available at <http://www.nature.com/reprints>.

1062

1063 **Extended Data Figure legends**

1064 **Extended Data Fig. 1. Inferring morphology of bogs with ditching.** Analysis of a bog cut
1065 by a ditch in Lost River peatland, Minnesota. Bog boundaries, lidar-derived surface
1066 elevations, and approximations to bog morphology from transforming the solution to
1067 Poisson's equation to bog surface elevations as in Fig. 1. Top: Analysis of peatland boundary,
1068 ignoring ditch. If the ditch is ignored, the rank-correlation between surface elevations and
1069 Poisson "elevations" is lower (0.98) because the assumptions underlying our approach are not
1070 valid in the ditch, where open-channel flow occurs. Bottom: Analysis of a subdomain that
1071 excludes the ditch, showing excellent agreement with the lidar topography ($\rho = 0.99$). The
1072 correlation coefficient is also improved (0.98 vs. 0.96) despite the smaller total relief within
1073 the subdomain boundary (2.45 m vs. 4.21 m) relative to microtopographic relief (~ 0.3 m).
1074 Satellite images: Google, Landsat / Copernicus.

1075 **Extended Data Fig. 2. Re-analysis of topography, time-averaged water table and**
1076 **hydraulic transmissivity in a dynamic model.** (a) Location of flowtube on the Mendaram
1077 bog for simulation shown in Fig. 7 of ref.⁷. Satellite image: CNES / Airbus, Google, Maxar
1078 Technologies. (b) Simulated water level, relative to local depressions, in the bog interior and
1079 at the bog margin, driven by recharge derived from weather station rainfall. The data intervals
1080 that are shown correspond to calendar years 2001, 2003 and 2007. (c) Minimum and
1081 maximum water tables within the flowtube for 2001, 2003, and 2007 (2007 overlies other
1082 years). (d) Distribution of water level for 2001, 2003, and 2007 (same colour scheme as b)
1083 for bog interior (solid) and margin (dashed); interior and margin time series are plotted in (b)
1084 but are not distinguishable. (e, f) Hydraulic transmissivity in the model as a function of water
1085 level (black line), and time-averaged transmissivity and water level along the flowtube
1086 (coloured points) in the three simulation years. (g) Average transmissivity divided by net
1087 recharge vs. surface elevation for 2001, 2003 and 2007. (h) Bog surface (black dashed line)

1088 and time-averaged water table $\langle H \rangle$ (coloured lines) vs. Poisson “elevation” ϕ for 2001, 2003
1089 and 2007 (2007 overlies other years).

1090 **Extended Data Fig. 3. Inferring morphology of bogs with incomplete elevation data. (a)**

1091 Milot: available elevation data exclude south-east corner of bog. **(b)** Mendaram: elevation

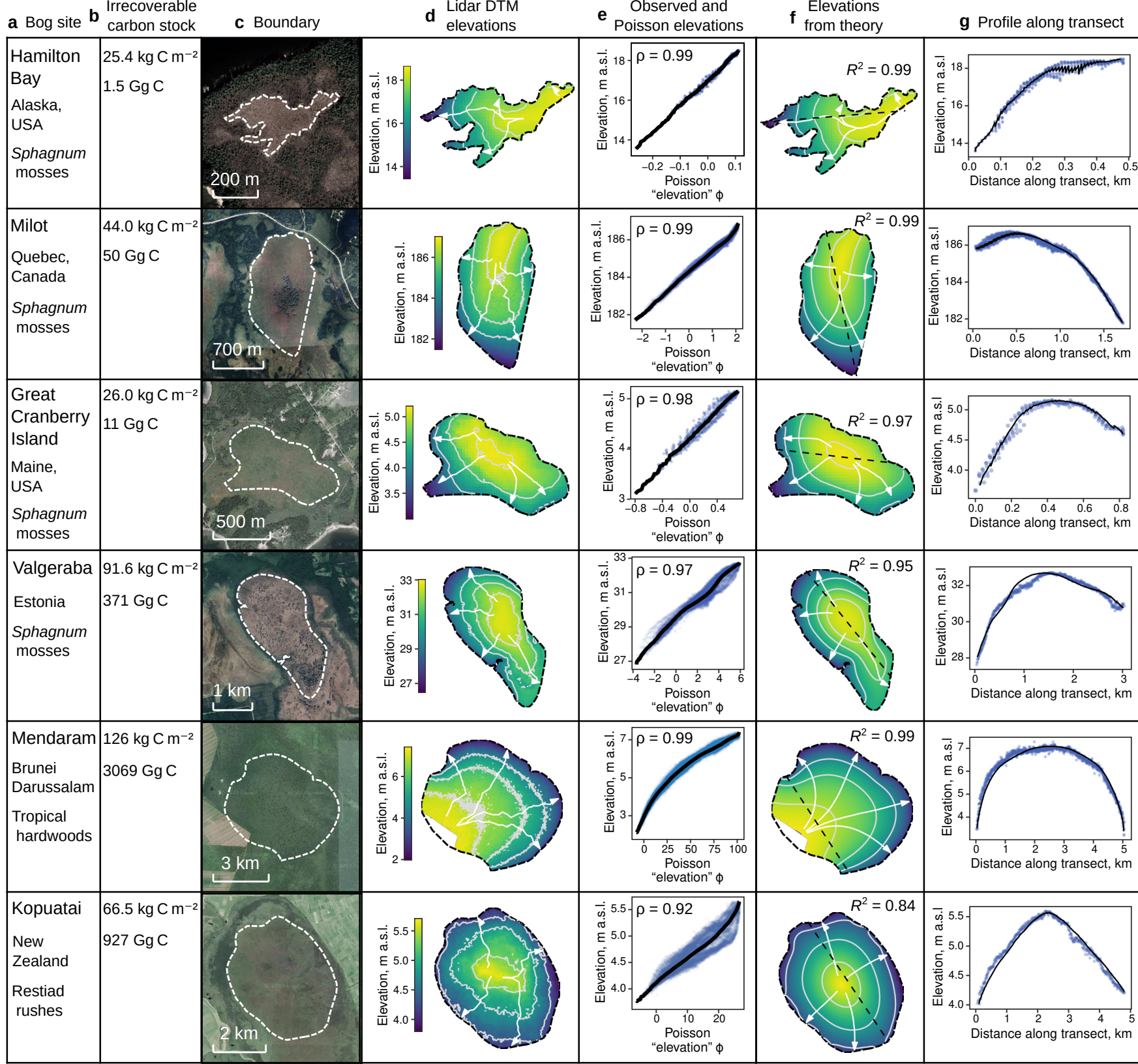
1092 data end at national boundary. **(c)** Rivers bounding Mendaram bog are obscured by floating

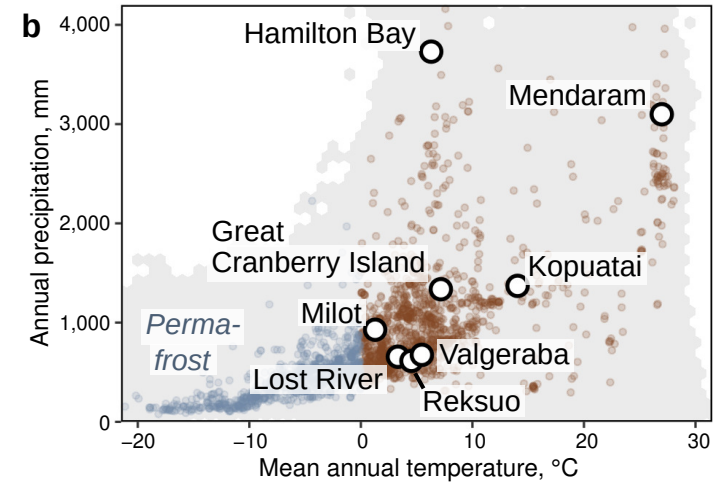
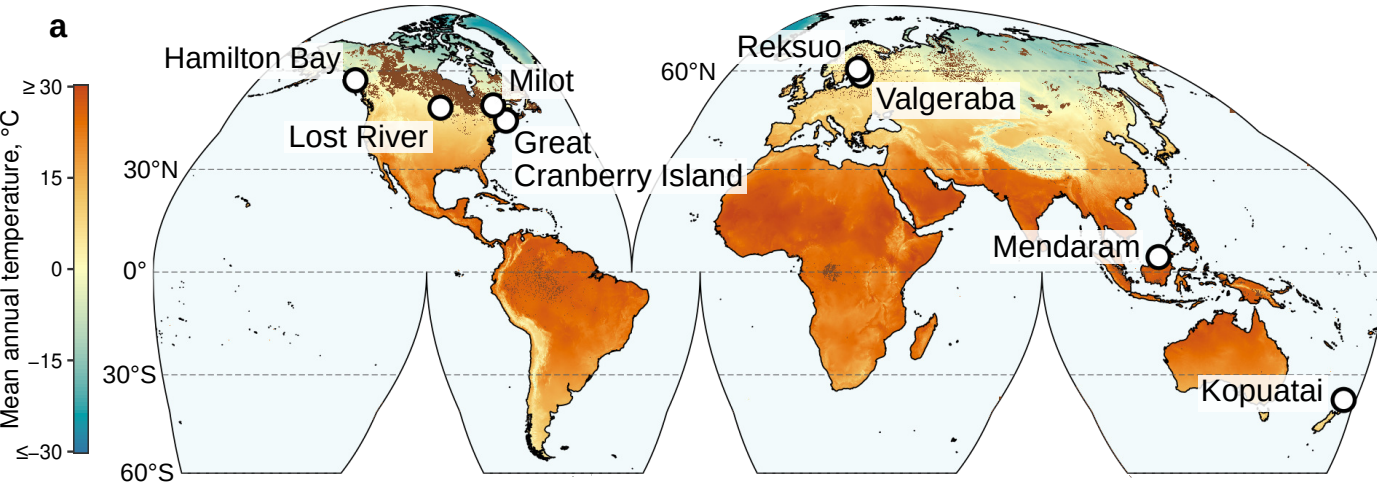
1093 vegetation, but visible in high-resolution images. **(d)** Estimated bog crest (groundwater

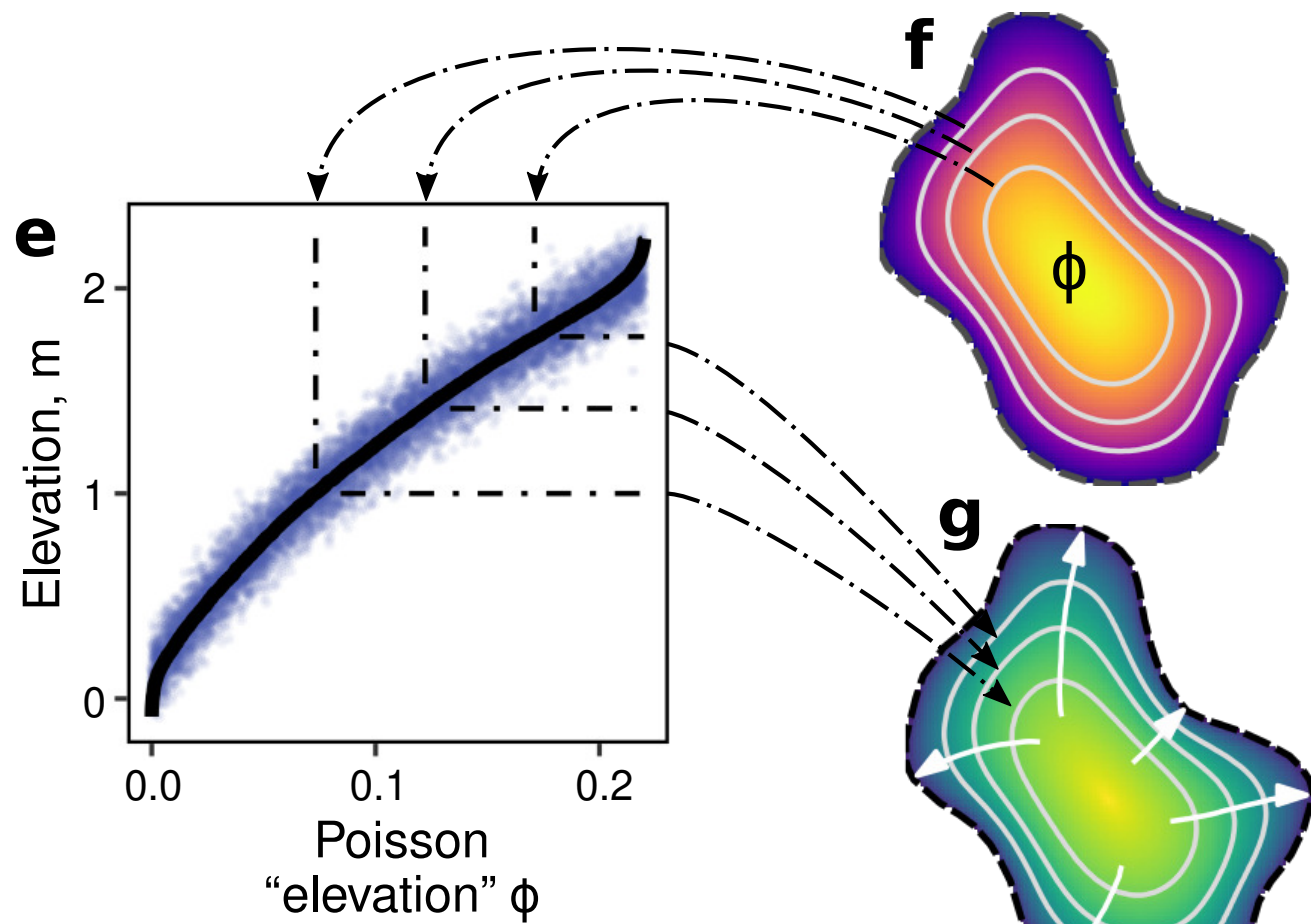
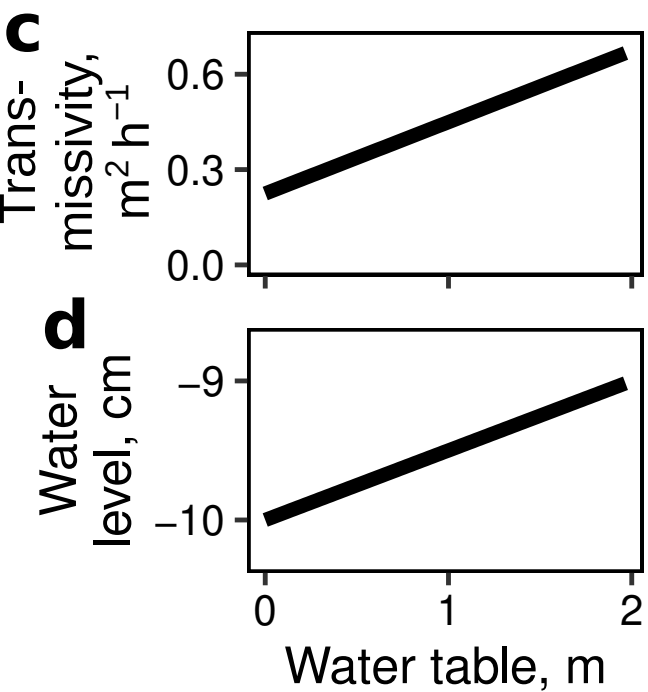
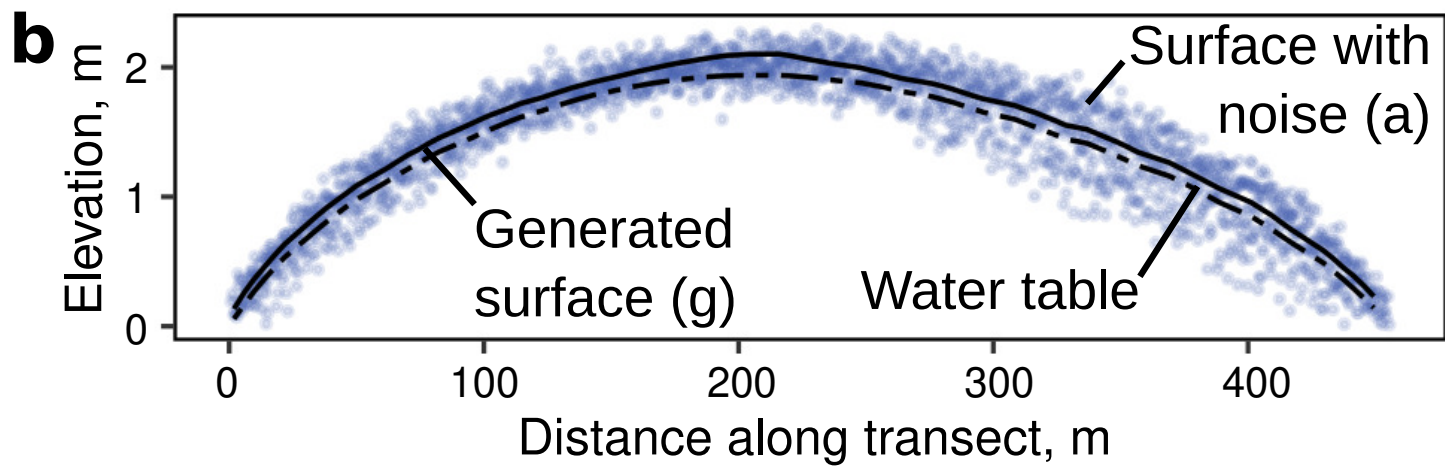
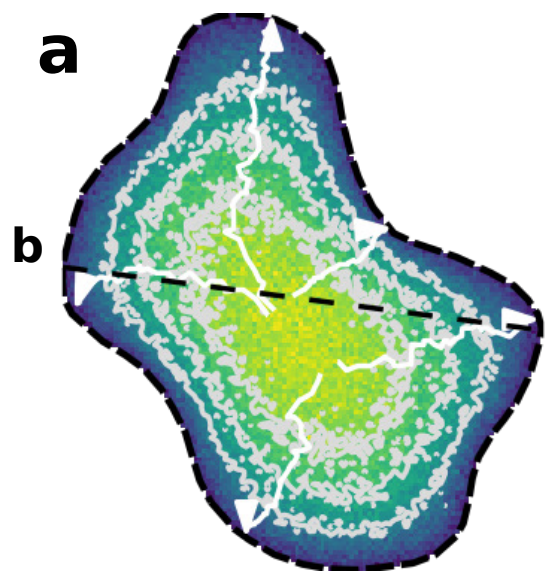
1094 divide) and flowlines used as no-flow (Neumann) boundaries. The location of the

1095 groundwater divide was estimated from available elevation data and the larger topographic

1096 setting **(b)**. Satellite images: CNES / Airbus, Google, Maxar Technologies.







Reksuo, Finland; 60.6°N, *Sphagnum*

